ELSEVIER

Nuclear Instruments and Methods in Physics Research A 437 (1999) 23–67

NUCLEAR INSTRUMENTS & METHODS IN PHYSICS RESEARCH Section A

www.elsevier.nl/locate/nima

The polarized double cell target of the SMC

The Spin Muon Collaboration (SMC)

D. Adams[a,1], B. Adeva[b,2], E. Arik[c,3], A. Arvidson[d,4], B. Badelek[d,e,5], M.K. Ballintijn[f,6,7], G. Bardin[g,8,9], G. Baum[h,10], P. Berglund[i], L. Betev[j,10], I.G. Bird[g,8,11], R. Birsa[k], P. Björkholm[d,12], B.E. Bonner[a,1], N. de Botton[g,8], M. Boutemeur[l,1,13], F. Bradamante[k], A. Bravar[m,10], A. Bressan[k,14], S. Bültmann[h,10,15], E. Burtin[g,8], C. Cavata[g,8], D. Crabb[n,1], J. Cranshaw[a,1,16], T. Çuhadar[c,f,3,6], S. Dalla Torre[k], R. van Dantzig[f,6], B. Derro[o,1], A. Deshpande[l,1], S. Dhawan[l,1], C. Dulya[o,1,17], A. Dyring[d,18], S. Eichblatt[a,1,19], J.C. Faivre[g,8], D. Fasching[p,1,20,21], F. Feinstein[g,8], C. Fernandez[b,q,1,2,20], S. Forthmann[r,10], B. Frois[g,8], A. Gallas[b,2], J.A. Garzon[b,q,1,2,20], T. Gaussiran[a,1], H. Gilly[s,10], M. Giorgi[k], E. von Goeler[t,20], S. Goertz[u,10], G. Gracia[b,2], N. de Groot[f,6,22], M. Grosse Perdekamp[o,1,23], E. Gülmez[c,3], K. Haft[j,10], D. von Harrach[m,10], T. Hasegawa[v,24,25], P. Hautle[w,26], N. Hayashi[v,24,27], C.A. Heusch[w,28],

* Corresponding author. Tel.: 071-521-0526; fax: 071-522-7178.
Email address: hpostma@dataweb.nl (H. Postma)

[1] Supported by the U.S. Department of Energy.

[2] Supported by Comision Interministerial de Ciencia y Tecnologia, Spain.

[3] Partially supported by TUBITAK and the Centre for Turkish-Balkan Physics Research and Application (Bogaziçi University).

[4] Now at The Royal Library, 102 41 Stockholm, Sweden.

[5] Supported by the Polish State Committee for Scientific Research (KBN) grant nr.2 P03B08114 and 2P03B13214.

[6] Supported by the National Science Foundation (NWO) of the Netherlands.

[7] Now at Rational Software Benelux, 2132 WT Hoofddorp, The Netherlands.

[8] Supported by the Commissariat à l'Energie Atomique, France.

[9] Deceased.

[10] Supported by the Bundesministerium für Bildung, Wissenschaft, Forschung und Technologie, Germany.

[11] Now at CEBAF, Newport News, VA 23606, USA.

[12] Now at Ericsson Infocom AB, Karlstad, Sweden.

[13] Now at University of Munich, Physics Department, 80799 Munich, Germany.

[14] Now at CERN, 1211 Geneva 23, Switzerland.

[15] Now at University of Virginia, Department of Physics, Charlottesville, 22901 VA, USA.

[16] Now at Texas Tech Univ., Lubbock TX79409-1051, USA.

[17] Now at CIEMAT, Avda Complutense 22, 28040 Madrid, Spain.

[18] Now at Swedish Space Corporation, 171 04 Solva, Sweden.

[19] Now at Fermi National Accelerator Laboratory, Batavia, 60510 Illinois, USA.

[20] Supported by the U.S. National Science Foundation.

[21] Now at University of Wisconsin, USA.

[22] Now at Bristol Univ., Bristol, UK.

[23] Now at Brookhaven National Laboratory, Upton, 11973 NY, USA.

[24] Supported by Monbusho Grant-in-Aid for Scientific Research (International Scientific Research Program and Specially Promoted Research), Japan.

[25] Permanent address: Miyazaki University, Faculty of Engineering, 889-21 Miyazaki-Shi, Japan.

[26] Permanent address: Paul Scherrer Institut, 5232 Villigen, Switzerland.

[27] Permanent address: The Institute of Physical and Chemical Research (RIKEN), wako 351-01, Japan.

[28] Permanent address: University of California, Institute of Particle Physics, Santa Cruz, 95064 CA, USA.

0168-9002/99/$ - see front matter
PII: S0168-9002(99)00582-3

N. Horikawa[v,24], V.W. Hughes[l,1], G. Igo[o,1], S. Ishimoto[v,24,29], T. Iwata[v,24], E.M. Kabuß[m,10], T. Kageya[v,24], A. Karev[x], H.J. Kessler[s,10], T.J. Ketel[f,6], J. Kiryluk[e,5], A. Kishi[v,24], Yu. Kisselev[x], L. Klostermann[f,6,30], D. Krämer[h,10], V. Krivokhijine[x], W. Kröger[w,28], K. Kurek[e,5], J. Kyynäräinen[h,i,10,31], M. Lamanna[k,14], U. Landgraf[s,10], T. Layda[w], J.M. Le Goff[g,8], F. Lehar[g,8], A. de Lesquen[g,8], J. Lichtenstadt[y,32], T. Lindqvist[d], M. Litmaath[f,6,19], M. Lowe[a,1,21], A. Magnon[g,8], G.K. Mallot[m,10], F. Marie[g,8], A. Martin[k], J. Martino[g,8], T. Matsuda[v,24,25], B. Mayes[q,1,20], J.S. McCarthy[n,1], K. Medved[x], W. Meyer[u,10], G. van Middelkoop[f,6], D. Miller[p,1,20], Y. Miyachi[v,24], K. Mori[v,24], J. Moromisato[t,20], J. Nassalski[e,5], L. Naumann[w,9], B. Neganov[x], T.O. Niinikoski[w], J.E.J. Oberski[f,6], A. Ogawa[v,24], C. Ozben[c,3], D.P. Parks[q,1,20], H. Pereira[g,8], A. Penzo[k], F. Perrot-Kunne[g,8], D. Peshekhonov[x,16], R. Piegaia[w,l,1,33], L. Pinsky[q,1,20], S. Platchkov[g,8], M. Plo[b,2], D. Pose[x], H. Postma[f,*,6], J. Pretz[m,10,34], T. Pussieux[g,8], J. Pyrlik[q,1,20], G. Rädel[w], I. Reyhancan[c,3], G. Reicherz[u,10], J.M. Rienbland[w], A. Rijllart[w], J.B. Roberts[a,1], S. Rock[w,35], M. Rodriguez[d,33], E. Rondio[e,5], A. Rosado[j,10], B. Roscherr[l,1], I. Sabo[y,32], J. Saborido[b,2], A. Sandacz[e,5], I. Savin[x], P. Schiavon[k], A. Schiller[r,10], K.P. Schüler[l,1,36], R. Segel[p,1,20], R. Seitz[m,10,37], Y. Semertzidis[w,23], F. Sever[f,6,38], P. Shanahan[p,1,19,20], E.P. Sichtermann[f,6], F. Simeoni[k], G.I. Smirnov[x], A. Staude[j,10], A. Steinmetz[m,10,34], U. Stiegler[w], H. Stuhrmann[r,10], M. Szleper[e,5], K.M. Teichert[j,10], F. Tessarotto[k], D. Thers[g,8], W. Tlaczala[e,5,39], S. Trentalange[o,1], A. Tripet[h,10], G. Unel[c,3], M. Velasco[p,1,14,20], J. Vogt[j,10], R. Voss[w], R. Weinstein[q,1,20], C. Whitten[o,1], R. Windmolders[z], R. Willumeit[r,10], W. Wislicki[e,5], A. Witzmann[s,1,40], A.M. Zanetti[k], K. Zaremba[e,5,39], J. Zhao[r,1,41]

[a]*Rice University, Bonner Laboratory, Houston, 77251-1892 TX, USA*
[b]*University of Santiago, Department of Particle Physics, 15706 Santiago de Compostela, Spain*
[c]*Bogaziçi University and Istanbul Technical University, Istanbul, Turkey*
[d]*Uppsala University, Department of Radiation Sciences, 75121 Uppsala, Sweden*
[e]*Soltan Institute for Nuclear Studies and Warsaw University, 00681 Warsaw, Poland*
[f]*NIKHEF, Delft University of Technology, FOM and Free University, 1009 AJ Amsterdam, Netherlands*

[29] Permanent address: KEK, Tsukuba-Shi, 305 Ibaraki-Ken, Japan.

[30] Now at Ericsson Telecommunication, 5120 AA Rijen, The Netherlands.

[31] Now at University of Jyväskylä, Dept. of Physics, FTN-40351, Jyväskylä, Finland.

[32] Supported by the Israel Science Foundation.

[33] Permanent address: University of Buenos Aires, Physics Department, 1428 Buenos Aires, Argentina.

[34] Now at Yale University, Department of Physics, New Haven, 06511 CT, USA.

[35] Permanent address: The American University, Washington D.C. 20016, USA.

[36] Now at DESY, Hamburg, Germany.

[37] Now at University of Montreal, H3C 3J7, Montreal, PQ, Canada.

[38] Now at ESFR, F-38043 Grenoble, France.

[39] Permanent address: Warsaw University of Technology, 00-665 Warsaw, Poland.

[40] Now at F.Hoffmann-La Roche Ltd., CH-4070 Basel, Switzerland.

[41] Now at Oak Ridge Nat. Lab., Oak Ridge, TN37831-6393, USA.

[g]C.E.A. Saclay, DAPNIA, 91191 Gif-sur-Yvette, France
[h]University of Bielefeld, Physics Department, 33501 Bielefeld, Germany
[i]Helsinki University of Technology, Low Temperature Laboratory and Institute of Particle Physics Technology, Espoo, Finland
[j]University of Munich, Physics Department, 80799 Munich, Germany
[k]INFN Trieste and University of Trieste, Department of Physics, 34127 Trieste, Italy
[l]Yale University, Department of Physics, New Haven, 06511 CT, USA
[m]University of Mainz, Institute for Nuclear Physics, 55099 Mainz, Germany
[n]University of Virginia, Department of Physics, Charlottesville, 22901 VA, USA
[o]University of California, Department of Physics, Los Angeles, 90024 CA, USA
[p]Northwestern University, Department of Physics, Evanston, 60208 IL, USA
[q]University of Houston, Department of Physics, and Institute for Beam Particle Dynamics, Houston, 77204 TX, USA
[r]GKSS, 21494 Geesthacht, Germany
[s]University of Freiburg, Physics Department, 79104 Freiburg, Germany
[t]Northeastern University, Department of Physics, Boston, 02115 MA, USA
[u]University of Bochum, Physics Department, 44780 Bochum, Germany
[v]Nagoya University, CIRSE and Department of Physics, Furo-Cho, Chikusa-Ku, 464 Nagoya, Japan
[w]CERN, 1211 Geneva 23, Switzerland
[x]JINR, Dubna, RU-141980 Dubna, Russia
[y]Tel Aviv University, School of Physics, 69978 Tel Aviv, Israel
[z]University of Mons, Faculty of Science, 7000 Mons, Belgium

Received 5 May 1999; accepted 31 May 1999

Abstract

The polarized target of the Spin Muon Collaboration at CERN was used for deep inelastic muon scattering experiments during 1993–1996 with a polarized muon beam to investigate the spin structure of the nucleon. Most of the experiments were carried out with longitudinal target polarization and 190 GeV muons, and some were done with transverse polarization and 100 GeV muons. Protons as well as deuterons were polarized by dynamic nuclear polarization (DNP) in three kinds of solid materials — butanol, ammonia, and deuterated butanol — with maximum degrees of polarization of 94%, 91% and 60%, respectively. Considerable attention was paid to the accuracies of the NMR polarization measurements and their analyses, the accuracies achieved were between 2.0% and 3.2%. The SMC target system with two cells of opposite polarizations, each cell 65 cm long and 5 cm in diameter, constitutes the largest polarized target system ever built and facilitates accurate spin asymmetry measurements. The design considerations, construction and performance of the target are reviewed.

Keywords: Dynamic nuclear polarization; Polarized protons and deuterons; NMR analysis

1. Introduction

An extensive programme to study the spin dependent structure functions of the nucleon has been carried out at CERN by the Spin Muon Collaboration (SMC). In the past few years results from the SMC measurements [1–8] from SLAC [9–16], and recently from HERMES [17] have improved our knowledge on the spin structure of the proton and neutron considerably.

In the SMC experiments, we made use of deep inelastic scattering (DIS) of longitudinally polarized muons off polarized protons and deuterons to study the internal spin structure of the nucleons. Since the secondary muon beam from the CERN SPS had a low flux (4×10^7 μ/pulse, pulse interval 14.4 s), and since the muon cross-section for scattering is small, a large polarized target with high spin density was essential to our measurements. Data taking by the SMC began in 1991 with the polarized target used by the European Muon Collaboration [18] as modified by the SMC for the first measurements with polarized deuterons [19].

Later data taking was carried out with a completely new polarized double cell target system. A short description of this SMC target has been

published [20]. Here we give a comprehensive report on the design of the SMC polarized target and on the experience gained from its operation during 1993–1996, with particular emphasis on the determination of the target polarization.

After a brief discussion in Section 2 of the method used to obtain the spin dependent structure functions, we describe in Section 3 the design, construction and operation of the polarized target system, in Section 4 the polarization measurements and analyses, and in Section 5 relaxation data and transverse polarization. In Section 6 we summarize our main results related to the SMC polarized target.

2. Basics of spin asymmetry measurements

The measurement of the spin-dependent structure functions $g_1^{p,d}$ of the proton and the deuteron provides vital information on the spin structure of the nucleon. Theoretical predictions exist for sum rules involving nucleon spin structure functions which can be tested using the results of polarized deep inelastic scattering experiments. In most of our measurements we determined the longitudinal spin asymmetry $A_{\parallel}^{p,d} = (\sigma^{\uparrow\downarrow} - \sigma^{\uparrow\uparrow})/(\sigma^{\uparrow\downarrow} + \sigma^{\uparrow\uparrow})$ for muon–nucleon scattering with the muon spin antiparallel and the target proton or deuteron spins parallel and antiparallel to the muon beam direction. For about 5% of our data taking, the transverse spin asymmetry $A_{\perp}^{p,d}$, corresponding to transverse nucleon spin orientations with respect to the scattering plane, was measured. These asymmetries are related to the proton and deuteron virtual photon asymmetries $A_1^{p,d}$ and $A_2^{p,d}$ according to

$$A_{\parallel}^{p,d} = D(A_1^{p,d} + \eta A_2^{p,d}), \quad A_{\perp}^{p,d} = d(A_2^{p,d} - \xi A_1^{p,d}) \tag{1}$$

in which the factors η and ξ depend only on kinematic variables and are small in our experiment, the depolarization factors D and d depend on kinematical variables and on the ratio $R = \sigma_L/\sigma_T$ of longitudinal and transverse photo-absorption cross sections.

Because of the small influence of $A_2^{p,d}$ in our longitudinal polarization measurements, the longitudinal asymmetry $A_{\parallel}^{p,d}$ can be related directly to the spin structure function $g_1^{p,d}$ by

$$g_1^{p,d}(x,Q^2) \approx \frac{F_2(x,Q^2)}{2x(1+R(x,Q^2))}\,\frac{A_{\parallel}^{p,d}}{D} \tag{2}$$

where $F_2(x,Q^2)$ is the unpolarized structure function, $-Q^2$ is the square of the four-momentum of the virtual photon exchanged between the muon and the target nucleon, and $x = Q^2/(2Mv)$ is the Bjorken scaling variable representing the fraction of nucleon momentum carried by the struck parton. Here M is the nucleon mass and v is the energy of the virtual photon. For a longitudinally polarized target the measured event yield, N, can be related to the longitudinal spin asymmetry

$$N = n\Phi a\sigma_0(1 - fP_{\mu}PA_{\parallel}) \tag{3}$$

where n is the number of target nucleons, Φ the beam flux, a the apparatus acceptance, σ_0 the unpolarized (i.e. spin averaged) cross-section, f the target dilution factor (defined in Eq. (6)), and P_{μ}, and P the beam and target polarizations, respectively. The asymmetry cannot be reliably extracted from two consecutive measurements with opposite target polarizations because the relative beam flux cannot be controlled with sufficient accuracy. Therefore, we have two oppositely polarized target cells in line along the beam, labelled "upstream" and "downstream", so that the two cells were exposed simultaneously to the same beam flux. The two cells of this target were separated by a suitable distance to allow identification of events coming from each cell.

For the measurement of $A_{\parallel}$ the ratio, $r = n_u a_u/n_d a_d$, occurs in which a_u and a_d are the apparatus acceptances for the upstream (u) and downstream (d) cells. Since r is not known the solution was to perform two consecutive measurements separated by a reversal of the polarization direction in both cells. Then the expression for the asymmetry becomes

$$A_{\parallel} = \frac{-1}{2fP_{\mu}P_t}\left(\frac{N_u - N_d}{N_u + N_d} - \frac{N'_u - N'_d}{N'_u + N'_d}\right) \tag{4}$$

where P_t is the weighed polarization of the two cells [7], N_u and N_d (N'_u and N'_d) are the number of DIS events from the upstream and downstream cells before (after) the polarization reversal. In this expression the ratio r cancels to a large degree if $r = r'$. A variation of r with time might occur due to a change in detector efficiencies. The difference $\Delta r = r - r'$ results in a systematic error

$$\Delta A_{\parallel} = \frac{1}{4 f P_{\mu} P_t} \frac{\Delta r}{r} \ . \tag{5}$$

In order to have $\Delta A_{\parallel}$ sufficiently small the target system was designed to allow frequent reversals of spins with little or no loss of target polarization.

For the measurement of $A_{\perp}$ it was also necessary to have the capability of rotating the polarization from the longitudinal to the transverse direction. The measurement of $A_{\perp}$ provides a value for A_2 which was needed to determine A_1 from $A_{\parallel}$ (see Eq. (1)).

It is important to obtain the highest possible degree of polarization. From a statistical error point of view an increase of the target polarization by a certain factor is equivalent to an increase of the number of events for a given running time by this factor squared (see Eq. (4)). Since the experiment aimed at a precise asymmetry measurement, for which systematic uncertainties were reduced to the order of 10^{-2}, the target polarization had to be known to this accuracy.

The polarized target system was designed with the above considerations in mind. In what follows we describe how the high degrees of polarization in the target cells were obtained and how these polarizations were measured accurately.

3. Design of the target

A solid polarized target has several important properties, in particular the inherently high and stable nucleon density and the high polarization obtained by using the technique of dynamic nuclear polarization (DNP) [21]. It is possible to obtain proton polarizations close to 100%. The polarization can be measured to a high accuracy.

DNP is obtained at temperatures below about 1 K, using a homogeneous magnetic field to polarize paramagnetic spins to a high degree, and a microwave field to transfer the polarization to the nuclear spins. For the samples used in our experiments DNP is not well described by the so-called "solid-state" effect in which for sufficiently dilute systems the interaction between paramagnetic spins can be neglected [22], but rather by the cooling (by microwave pumping) of the paramagnetic spin–spin interaction "reservoir" [23]. Therefore, the nuclei become polarized by the coupling of the nuclear spin and the paramagnetic spin systems. Nuclear spin relaxation must be orders of magnitude slower than the relaxation of the dilute paramagnetic centres so that the latter are used repeatedly to flip the nuclear spins into the preferred direction. Spin diffusion is an additional important phenomenon in this process. Depending on the tuning of the microwave frequency the proton or deuteron spins become polarized parallel or antiparallel to the magnetic field.

The low intensity muon beam and the small muon–nucleon cross-section made it necessary to use a thick target. On the basis of the argument given in Section 2 we designed a target with two cells in line, each 60 cm (later 65 cm) long separated by 30 cm (later 20 cm). The target diameter was 5 cm consistent with the expected muon beam profile. A superconducting solenoid was designed to provide a very homogeneous longitudinal field over at least 150 cm. The field strength chosen was 2.5 T which allowed us to use two available microwave sources of about 70 GHz. A saddle type coil was superposed on the solenoid coil to produce a dipole field of 0.5 T perpendicular to the solenoid field and to enable (1) a relatively fast and reliable reversal of the nuclear spins by field rotation about 180°, and (2) after DNP in the solenoid field to rotate the polarization in a field of 0.5 T from the longitudinal to the transverse direction. With the spins in a field of 0.5 T with the microwaves off, it is necessary to have a target temperature well below 0.1 K in order to achieve long relaxation times. Therefore, a dilution refrigerator was designed (1) to absorb a large amount of microwave power of about 1 W during DNP at about 0.5 K, and (2) to cool the large amount of target material rapidly to well below 0.1 K after the microwave power is turned off. Fig. 1 shows the lay-out of the

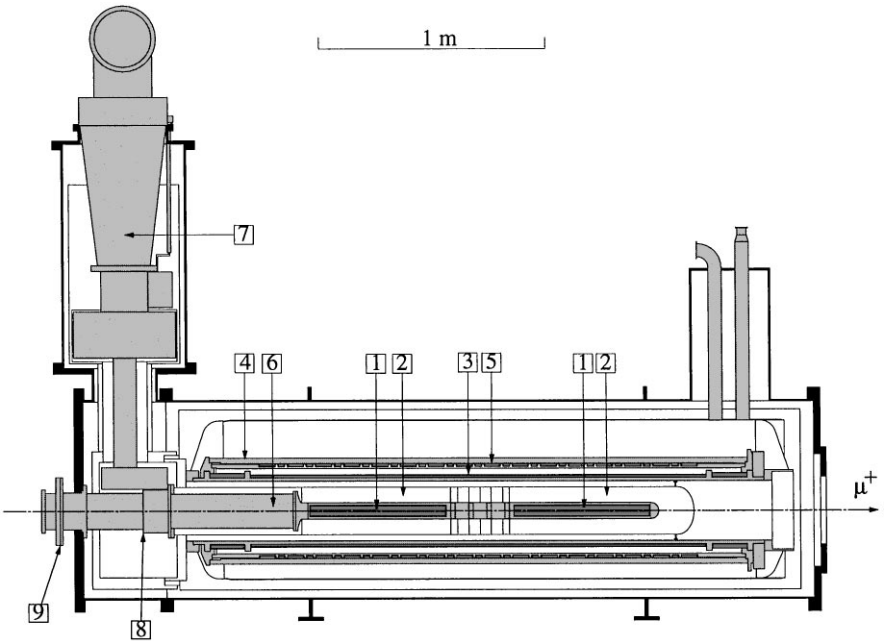

Fig. 1. The SMC target cryostat with the target holder as used in 1993. The muon beam traverses the cryostat from left to right. (1) Target cells, (2) microwave cavity, (3) solenoid coil, (4) dipole coil, (5) correction coils, (6) dilution refrigerator, (7) precooler of ^{3}He, (8) indium seal, and (9) external seal.

dilution refrigerator and the magnet system of the target.

A nuclear magnetic resonance (NMR) system with 10 coils was designed to determine the polarizations in the two target cells. To achieve accurate and reliable determinations of the degree of polarizations over the complete target volume is challenging and much attention was paid to the design of the NMR coils, of cabling to the electronics, of the electronic NMR units and to the analysis of the NMR signals.

In the following, we discuss the technical realization of the main components of this double cell polarized target system, including the material, the dilution refrigerator, the magnets, the microwave system and the NMR system. A detailed discussion is given of the systematic uncertainties in the polarizations for the different target materials.

3.1. Target materials

In the case of polarized solid-state targets unpaired electron spins with a density in the range of 10^{19}–10^{20} cm^{-3} are needed for the DNP process to work well. Depending on the material, these can be introduced by chemical doping with a paramagnetic compound or by irradiation which creates free radicals. In the SMC experiment the radiation damage due to the low-intensity muon beam was negligible and did not limit the choice of material. Both methods of introducing unpaired electrons were used. In 1993, butanol (C_4H_9OH) with a paramagnetic complex was used as a proton target, in 1994 and in 1995, deuterated butanol (C_4D_9OD) with a paramagnetic complex as a deuteron target, and in 1996, irradiated ammonia (NH_3) again as a proton target.

The dilution factor f is defined in our case as the fraction of events scattered off the polarizable nucleons under study,

$$f = \left(1 + \sum_A \frac{n_A \cdot \sigma_A}{n_{\mathrm{p(d)}} \cdot \sigma_{\mathrm{p(d)}}}\right)^{-1} \quad (6)$$

where n is the number of nuclei and σ the unpolarized scattering cross-section per nucleus

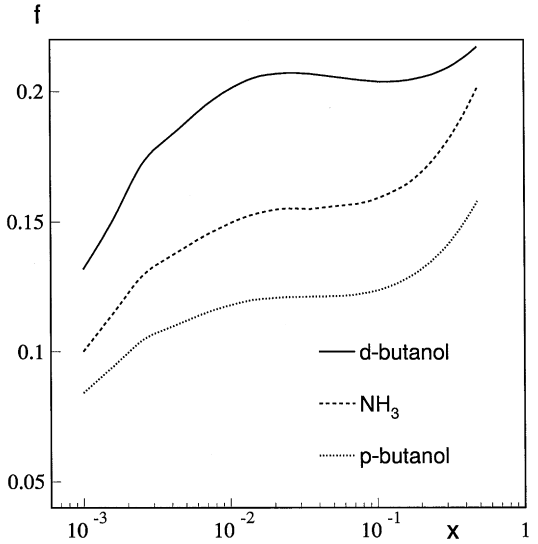

Fig. 2. The dilution factors f for the different target materials as function of Bjorken x. The curves (from top to bottom) correspond to deuterated butanol, ammonia and butanol.

(proton, deuteron or elements with the atomic weight A). Due to different dependencies of σ_A and $\sigma_{p,d}$ on the Bjorken-x, the dilution factor varies with x as is shown in Fig. 2 for the three target materials. In addition to the target material, the dilution factors depend on the ^{3}He/^{4}He cooling mixture, whose composition varied with temperature, and on the embedded NMR coils with their support structure. The amounts of the elements in each cell are given in Table 1.

Butanol is a clean material in the sense that the background carbon and oxygen nuclei are spinless (except for abundances of 1% for ^{13}C and 0.3% for ^{17}O), but f is relatively small. Paramagnetic centres are introduced by dissolving a suitable compound. Ammonia has a larger dilution factor, but has the drawback that the spin-1 ^{14}N nuclei introduce a polarized background which must be corrected for. Solid ammonia was irradiated at $\sim$80 K with 20 MeV electrons to introduce the paramagnetic radicals. The use of $^{15}NH_3$ with spin-$\frac{1}{2}$ ^{15}N nuclei was not feasible in our experiment because of the high cost of the material. Deuterated ammonia has a higher dilution factor than that of deuterated butanol, but requires a secondary irradiation at 4 K inside the target system in order to obtain high polarization [24], which was not possible in our experimental situation.

To compare the two proton target materials we consider the statistical errors of the spin asymmetries, which are inversely proportional to $\sqrt{x_m \rho f P}$, assuming that the target volume and beam flux are the same. Here x_m is the packing fraction, ρ is the density and P is the average target nuclear polarization. Using the values of the parameters given in Table 2, it is found that the

Table 1
The elements and their respective moles of the target materials

Element	Material		
	Butanol n_A (mole)	d-Butanol n_A (mole)	Ammonia n_A (mole)
^{1}H	185.7	1.2	226
^{2}H	—	206.2	—
^{3}He	6.5 ± 1.0	4.7 ± 1.0	5.4 ± 1.0
^{4}He	23.6 ∓ 1.5	26.6 ∓ 1.5	30.7 ∓ 1.5
C	71.8	80.2	0.22
N	—	—	75.4
O	22.7	25.1	—
F	0.24	—	0.45
Na	0.17	0.18	—
Cr	0.17	0.18	—
Ni	0.14	[a]	0.25
Cu	0.36	[a]	0.58

[a] In 1994 the NMR coils were not embedded in the material.

Table 2
Typical parameter values for butanol and ammonia target materials

	Packing fraction x_m	Density ρ at 77 K (g/cm^3)	Dilution factor $\langle f \rangle$	Polarization P_{av} (yr)
Butanol	0.62 ± 0.04	0.985	0.12	0.86 (1993)
Ammonia	0.58 ± 0.01	0.853	0.15	0.89 (1996)

statistical error for the ammonia target is reduced by a factor of 0.83 in comparison to a butanol target. This gain in accuracy is due to the larger value of the dilution factor, despite the lower packing fraction and the lower density of ammonia. The low packing fraction is due to the irregular shape of the ammonia chips and the low density of ammonia which made it difficult to fill the long target cells, because the chips tended to float on the liquid nitrogen during loading (see Section 3.2).

3.1.1. Preparation of normal and deuterated butanol

The butanol material was doped by dissolving in it the paramagnetic complex EHBA–Cr(V) [25,26]. The mass composition by weight of the target material was 78.5% 1-butanol, 12% 2-butanol, 5% water, and 4.5% EHBA–Cr(V) for the normal butanol material. For the deuterated butanol material 91.4% 1-butanol, 4.6% water, and 4% EHBA–Cr(V) was used, for which the components were taken in their perdeuterated form. The deuteration level of this target material was 99.4%. Water was added to promote glass formation, necessary to obtain a homogeneous distribution of the dopant. Together with a uniform cooling of the material, this was crucial for a homogeneous distribution of the polarization. The liquid mixture of the deuterated butanol and its additives was solidified into spherical beads of 1.8 mm diameter by dropping the liquid solution through a needle onto the surface of a liquid nitrogen bath. The droplets of 3 μl volume froze within 4–5 s and then sank to the bottom of the bath. An apparatus [27] was built to obtain a fast production of the needed quantity of around half a million beads. For that purpose the liquid nitrogen bath was constructed with separate compartments, which moved in succession under two dripping needles. A similar procedure was used for the normal butanol material resulting in beads of 1–3 mm diameter. Detailed studies of the butanol target materials were carried out [27]. The low-temperature densities of butanol and deuterated butanol materials were measured to be 0.985 ± 0.031 g/cm^3 and 1.106 ± 0.012 g/cm^3, respectively.

3.1.2. Preparation of ammonia

For the 3 l of solid ammonia which had to be prepared for this experiment, a new solidification apparatus with a continuous cooling system was built. The solidification proceeded as follows. Ammonia gas was first condensed in a glass tube at 240 K using an ethanol bath cooled by cold nitrogen gas. When the ammonia gas flow was switched off after about 150 cm^3 of ammonia was liquified, the material immediately started to freeze at the tube wall. Filling the glass cylinder with 500 mbar of argon allowed the liquid to freeze very homogeneously to form a transparent block of ammonia ice. It was then crushed into pieces under liquid nitrogen and sifted to 2–3 mm chip size.

To create $\dot{N}H_2$ radicals [28] by irradiation at a low temperature, the sample was immersed in a liquid argon bath at 87 K using a cryostat of which an initial version is described in Ref. [29], but with some modifications in order to guarantee constant conditions for the irradiation of the whole amount of the target material [30].

The irradiation was performed at the Bonn University with 20 MeV electrons and a beam current of 30 μA. The charge collected by the sample container was used as a relative measure for the density of the implanted paramagnetic centres. The constraint of dose homogeneity limited the batch size to 150 cm^3. The geometry of the container and the rotation of the sample produced a sufficiently homogeneous irradiation of the material. This could be judged from the uniform blue colour of the material after the irradiation as well as from the similar polarization behaviour of different small samples which were tested. The density of paramagnetic centres was estimated to be 6×10^{19} cm^{-3} from previous measurements [28].

3.2. The dilution refrigerator

Dilution refrigeration [31] was the only practical method for cooling our target because temperatures well below 100 mK were required to sufficiently slow down the spin-lattice relaxation at 0.5 T and thereby to rotate the magnetic field (see Section 3.3) with minor loss of polarization. In addition, this made it possible to carry out transverse spin asymmetry measurements with a 0.5 T field. Furthermore, higher polarizations were obtained about 200 mK, a region inaccessible to evaporation refrigerators.

3.2.1. Basic requirements

The structure of the refrigerator was dictated by the following requirements: (1) to have a minimum amount of structural material in the muon beam, (2) to allow loading of the target material precooled below 100 K, (3) to have it fit inside the superconducting magnet, and (4) to provide large cooling power needed for DNP. A flow-type cryostat was chosen instead of a bath-type to obtain faster operation. A special feature was the possibility to load the target material at 77 K directly into the mixing chamber. The design of the SMC dilution refrigerator is largely based on that of the EMC polarized target set-up [32,33]. Fig. 1 shows a cross-section of the target cryostat.

3.2.2. Technical solutions

The purpose of the elaborate precooling system was to reduce the ^{4}He boil-off rate to provide a safe margin to the helium liquifier which had a maximum capacity of 100 l/h and which also had to supply the magnet system. A 2000 l liquid helium dewar, installed between the liquifier and our refrigerator plus magnet, served as a buffer. The liquid ^{4}He consumption of the refrigerator varied between 15 and 40 l/h depending on the ^{3}He flow rate. The flow of liquid ^{4}He into the evaporator (volume 27 l) was regulated by a motor-driven needle valve coupled to a capacitive level gauge inside the evaporator and thus maintained the liquid helium level within preset narrow limits.

3.2.3. Heat exchangers

The concentrated ^{3}He flow, going from the still to the mixing chamber, was first cooled in a tubular heat exchanger followed by a series of sintered copper heat exchangers. They were placed inside a helicoidal groove, machined in glassfibre-epoxy cylindrical spacers between two stainless steel tubes. The groove defined the dilute ^{3}He phase flow channel. The tight fitting of the outer stainless steel tube to the glassfibre-epoxy spacers sealed off this flow channel. The calculation of the required surface area in these heat exchangers was based on information given in Ref. [34]. The tubular heat exchanger was made of flattened stainless steel tubes and had a total surface area of 0.1 m^2. Since the refrigerator had to provide high cooling powers at about 0.3 K, the effective surface area could not be increased by increasing the sinter thickness, because the transverse heat conduction in the helium and in the sinter limits the heat transfer. Instead, we had to rely on increasing the interfacial surface area between the sinter and the fluid streams. For the same reason, copper sinter was preferred over silver. The sintered heat exchangers were arranged in two parallel streams. To prevent cold plug formation due to the increasing viscosity of ^{3}He below 0.5 K, the flow in the streams was crossed at several points. The heat exchanger elements consisted of two sintered copper plates which were first bent to fit into the flow channel and then electron-beam welded together. The average thickness of the layer of the nominally 18 μm grain size sinter was 0.75 mm, yielding 375 g of sinter and a geometrical surface area of 12 m^2 on both the concentrated and the dilute phase streams. The heat transfer was enhanced by grooves in the sinter surface to increase the interfacial area with fluid flow and to produce turbulence in it.

3.2.4. Mixing chamber and target holder

The mixing chamber, with a length of 1600 mm and a diameter of 70 mm, was made of glassfibre-reinforced epoxy with 0.6 mm wall thickness to ensure sufficient rigidity and to withstand overpressure in the case of a pump failure. The target holder could slide into the horizontal access tube and was internally connected with a cold indium seal to the dilution unit at position 8 indicated in Fig. 1. A vacuum chamber at the entrance side of the target holder had two 0.1 mm stainless steel windows for the beam access and 6 aluminium foil thermal shields, and it provided thermal anchors for the coaxial cables for the NMR coils and for the instrumentation wires of the cryogenic sensors inside the mixing chamber.

The target support was made mainly of kevlar–epoxy composite for lightness, rigidity, and small thermal contraction. The target material was located in two cells of earlier given dimensions. Good heat transfer was assured by making the cells out of polyester net with 60% of open area. To ensure uniform cooling, liquid ^{3}He was fed into the mixing chamber through 40 holes in a CuNi tube which was fixed to the target holder.

A spring-loaded conical connector coupled the outlet of the heat exchanger to the CuNi tube when the target holder was in place.

3.2.5. Pumping system

A pumping system for ^{3}He, available from the EMC experiment, with 8 Root's blowers[42] in series was used, giving a volume speed of 13500 m^3/h. Charcoal traps at room temperature and at 77 K were used to filter out impurities in the ^{3}He return flow, in addition to the zeolite filters in the pumps. The amount of ^{3}He gas for normal operation of the dilution refrigerator was 800 l (at standard temperature and pressure). The ^{3}He + ^{4}He mixture was stored at room temperature and with 0.5 bar overpressure.

3.2.6. Microwave cavity

The mixing chamber was surrounded by a cylindrical copper microwave cavity of 210 mm diameter. The cavity was divided axially into two compartments by a microwave stopper. It was designed to ensure inside the mixing chamber free diffusion and convection in the dilute solution (see also Section 3.4). The cavity was cooled to 3 K by ^{4}He flow controlled by a cold needle valve. The two wave guides feeding two sections of the cavity had FEP plastic windows to seal the main vacuum and to isolate the cavity in order to prevent loss of ^{3}He in case of a rupture of the mixing chamber.

3.2.7. Thermometry

Temperature measurements below about 10 K were based on carbon and RuO resistors, read by 4-wire AC resistance bridges.[43] The resistors in the mixing chamber were partly shielded against the microwave field. Higher temperatures were measured with silicon diodes. During the calibration of the NMR system, the refrigerator was filled with pure ^{4}He at a temperature of about 1 K. This temperature was measured with a ^{3}He vapour pressure bulb inside the mixing chamber.

Between 0.5 and 5 K the international temperature scale ITS-90 is based on the saturated vapour pressure of ^{3}He, whose measurement provided therefore the most accurate and straightforward determination of the temperature of the target material during NMR calibration runs. For this purpose a high precision capacitive pressure gauge was used.[44]

3.2.8. Computer interface

A graphical user interface was running on a Unix workstation[45] and could be displayed on several X-terminals, while the control program was running in a VME processor. More than 100 cryogenic parameters were logged by the programs which also generated alarms [35]. Most readout instruments were read via a GPIB bus, either directly or using a 32-channel data logger and plotter.[46]

3.2.9. Operation and performance

During DNP the temperature of the helium mixture decreased slowly from about 350 to 200 mK (400 to 300 mK in case of the ammonia target) as the optimum microwave power reduced with increasing polarization. The target was cooled down well below 100 mK by turning the microwave power off 0.5–1 h before field rotation. A memory effect was observed: after long microwave irradiation with high power the upstream target cooled down more slowly than the downstream one. This was attributed to conduction of heat from the microwave stopper to the mixing chamber, because the stopper slightly touched the mixing chamber.

The cooling power in the mixing chamber with optimum ^{3}He circulation is shown in Fig. 3. The temperature was measured at the outlet of the dilute phase from the mixing chamber. A residual heat leak of about 1.4 mW to the mixing chamber was mainly from this end. At this position the temperature was 20–30 mK higher compared to the downstream end where the lowest temperature of 30 mK was obtained. The ^{3}He flow rate had practical minimum and maximum values of 27 and 350 mmol/s with a ^{4}He content of about 25% in the pumped ^{3}He gas due to the rather high still temperature of 0.95 K.

[42] Pfeiffer Vacuum GmbH.

[43] AVS-46 by RV-Elektroniikka Oy.

[44] MKS Baratron 270B.

[45] SUN SparcStation10.

[46] Siemens Multireg C1732.

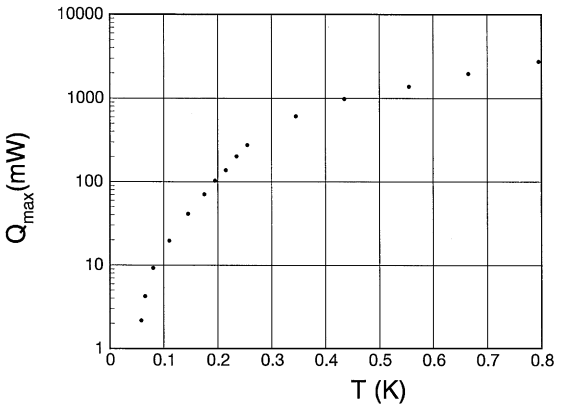

Fig. 3. The maximum cooling power Q_{max} versus the mixing chamber temperature T.

3.2.10. Target loading

One of the design features of this refrigerator is that it could be loaded with both the target and refrigerator well below 100 K. To stay well below 100 K during loading was extremely important since the target materials have critical temperatures in the range of 100–120 K related to devitrification or to the decay of radicals in ammonia. The loading of the refrigerator with the target material was a delicate operation, but could be accomplished reliably as follows. At the start, the empty target holder was submerged in a long bath filled with liquid nitrogen. The two cells of the target holder were filled under liquid nitrogen with the target material stored at 77 K. At this point the dilution refrigerator was precooled to about 4 K. The space into which the target holder was to be inserted, was covered with a quickly removable plate and was filled with helium gas. The filled target holder was lifted from the liquid nitrogen bath and slid into the dilution refrigerator within less than a minute. Two heavy external clamps were used to rapidly compress the inner indium O-ring with sufficient force to provide proper sealing of the dilution refrigerator at the back wall of the still. The indium seal was further tightened with bolts and the external flange was sealed. Finally, the dilution refrigerator was evacuated and purged several times with helium gas during a couple of hours to remove the remaining liquid nitrogen from the target.

3.3. The superconducting magnet system

As described in the introduction of this section a 2.5 T magnetic field was chosen for DNP which also requires a field homogeneity better than 10^{-4} throughout the target volume to reach a uniform polarization.

The magnet [36] consists of three concentric coil systems: a main inner solenoid with a compensation coil at each end, an assembly of 16 correction coils distributed along the solenoid and an outer dipole of saddle coil type. The dimensions and electrical characteristics of these subsystems can be found in Table 3. The magnets were immersed in a liquid helium bath which was thermally isolated by a radiation shield, cooled by the evaporating helium, and by multilayer superinsulation. The magnet current leads, which passed through three separated tubes, were cooled in the same way. There were no persistent mode switches because

Table 3
Dimensions and electrical parameters of the magnet windings

	Solenoid and compensation coils	Correction coils	Dipole
$\varnothing_{inner}/\varnothing_{outer}$ (mm)	300/326 to 347	408/414 to 422	500/508
Length (mm)	$2000 + 2 \times 150$	150	2500
Conductor	Cu–NbTi	Cu–NbTi	Keystone Rutherford
Nominal B (T)	2.5	—	0.5
$\Delta B/B$	$< 2 \times 10^{-5}$		$\leqslant 2 \times 10^{-2}$
Nominal I (A)	416	$\leqslant 8$	650
dI/dt_{max} (A/s)	0.5	—	2.5
Inductance (H)	5.6	0.06 to 0.54	0.4
Discharge resistor (Ω)	1	—	0.4

the current had to be frequently changed for the reversal of the spin directions.

The solenoid field was aligned parallel to the muon beam. With the help of the correction coils, a homogeneity better than $\Delta B/B = 3.5 \times 10^{-5}$ could be reached over the full cylindrical volume of the target cartridge (1500 mm long and 50 mm in diameter). This number was deduced from the distribution of the NMR line centres among the 10 coils. The magnet system alone, i.e., without the target, reached a homogeneity of 2×10^{-5} which was obtained by the use of wet winding technique, aided by an automatic wire positioning guide. A 0.5 T maximum vertical dipole field was perpendicular to the main solenoid field. It was used to maintain polarization during the rotation of the spins and also during measurements with transverse target polarization. Since this magnet was used for neither DNP nor NMR, a 2% field homogeneity was sufficient.

The two-mode hardware security system could generate fast or slow discharges of the magnets. The slow discharge mode reduced the stress on the magnet compared to that caused by a fast discharge. If the temperature or the voltage of the current leads had increased too much or if a quench had been detected, then the coils would have been automatically disconnected from their power supplies. The solenoid and the dipole would have then quickly discharged through a 1 Ω and a 0.4 Ω resistor, respectively; these resistors were located inside the helium bath above the liquid level. In case of less serious incidents such as bad isolation vacuum, low helium flow in the current leads or low helium level inside the cryostat, the magnets were slowly discharged through the power supplies in about 10 min. The security system also inhibited the dipole magnet to be on when the solenoid field was larger than 0.5 T, since this could mechanically damage the magnets.

The magnets were controlled from the same Unix workstation as used for the dilution refrigerator, and a VME crate with a CPU[47] running under the VxWorks[48] operating system. The interfaces with the instruments were made with 8 or 16 channels 12-bit DAC boards, 12-bit ADC boards, and a digital input/output board for 96 channels;[49] most channels were optically isolated by a signal conditioner. The solenoid current supply[50] was directly read and controlled by the CPU through a RS232 line, while the dipole[51] and correction coil current supplies[52] were controlled through a DAC and read by an ADC. The ADC's were also used to read magnet cryogenic parameters. The VME crate was connected to the work-station through a private Ethernet. The work-station provided development capabilities and a graphical user interface.[53]

An automatic rotation procedure was developed, in which the solenoid field was ramped from ± 2.5 to ∓ 2.5 T in order to reverse the spins. To ensure that the total magnetic field remained above 0.5 T during rotation, the dipole field was ramped up to 0.5 T and back to zero during the time when the solenoid field was below 0.5 T. The polarity of the correction coils was reversed when the solenoid field was zero. The rotation required about 35 min. During most of this time the muon beam could stay on, except for a 10 min period when the dipole was turned on.

In the beginning of the 1993 proton data taking, a considerable loss of the negative polarization due to superradiance [37,38] was observed during rotation. To suppress this effect and to save the polarization, the field was made inhomogeneous during the rotation procedure by applying suitable currents to the correction coils (see Section 4.5). This cured the problem completely.

3.4. The microwave system

The desired opposite spin directions in the target cells required two independent microwave sources operating near 70 GHz at the lower and upper edges of the paramagnetic spectrum with a spacing

[47] Matrix MDCPU334.
[48] Wind River Systems.
[49] ADAS ICV712, ICV150 and ICV196.
[50] Drusch M1281.
[51] Drusch M1349.
[52] Euro-Test LAB/S110.
[53] SL-GMS by Sherrill-Lubinski Co.

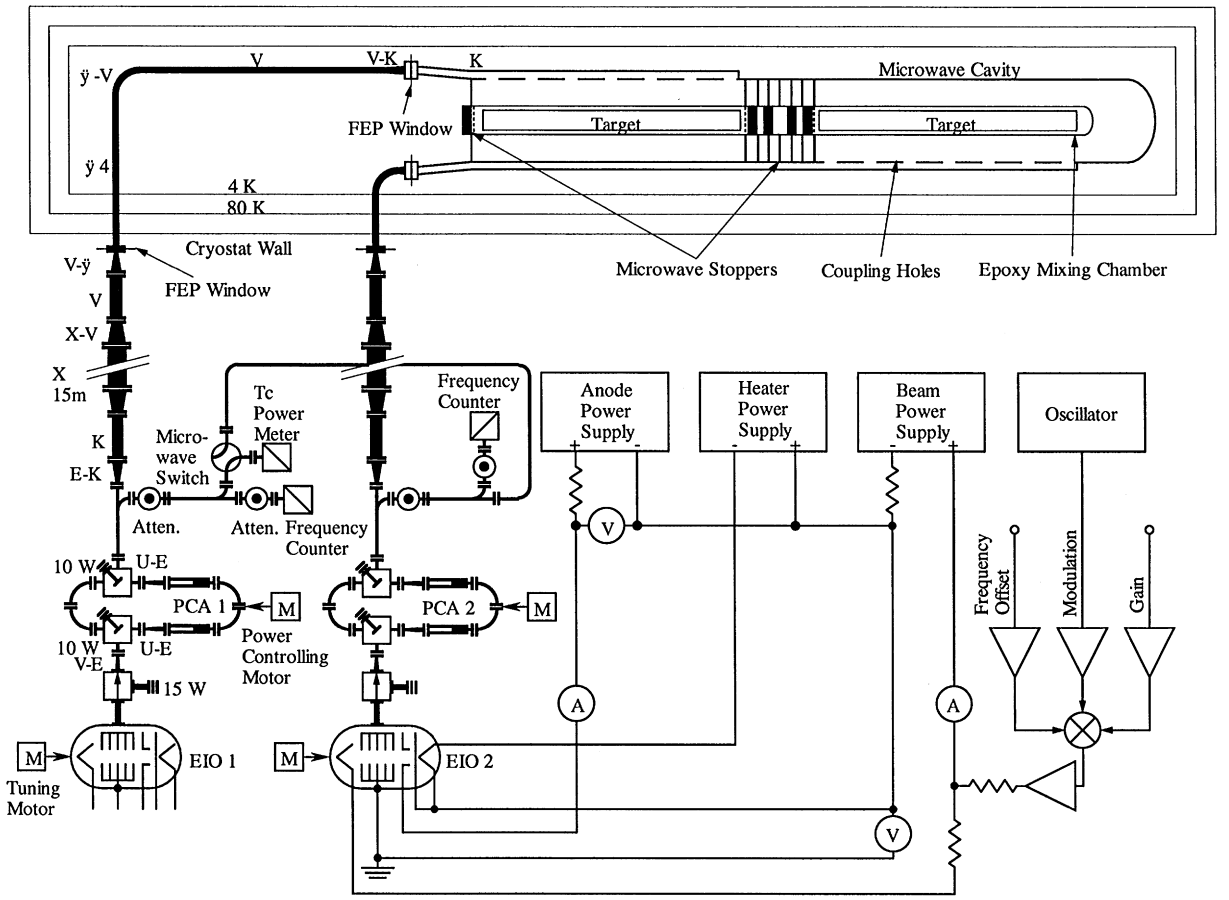

Fig. 4. The microwave instrumentation.

of about 0.4 GHz. The frequency and the power output of the microwave sources had to be fine-tuned during DNP. Fig. 4 shows the main parts of the microwave system.

The microwave power was generated by two extended interaction oscillator (EIO) tubes,[54] delivering up to 20 W of continuous power in a band of about 2 GHz around 70 GHz. The frequency could be set coarsely by changing the cavity size of the EIO, and fine-tuned by adjusting the cathode voltage of the HV power supply.[55] The coarse frequency change was used for changing the polarization sign of the target cells, while the electrical tuning by the cathode voltage enabled fine control of the frequency by 0.25 MHz/V within a band of about 200 MHz. In addition, a triangular waveform was applied to the cathode voltage in order to modulate the microwave frequency in a band of 30 MHz at a rate of about 1 kHz in order to improve the speed of polarization and to obtain a higher degree of polarization (see Section 4.6).

The sources were protected against reflected microwave power by circulators, equipped with 15 W matched loads. Two power control attenuators (PCA) [39,40] were used to regulate the microwave power to the two target halves.

[54] Varian VKE 2401.
[55] Siemel type CO.

The maximum power rating of commercially available microwave attenuators operating at 4 mm wavelength is only a few watt, while in our circuit the attenuators had to withstand power levels of 15 W. Our PCA's consist of two hybrid tees, waveguides, and matched loads arranged in a trombone-like structure as can be seen in Fig. 4. The incoming microwave is divided by the first hybrid tee into two waves; one is directed to one arm of the PCA with a motorized sliding waveguide with the shape of a trombone, and the other wave is going through a fixed waveguide in the other arm. The sliding waveguide acted as a phase shifter when moving the inner waveguide with respect to the outer one thus altering the electrical length. The two waves are combined in the second hybrid tee. When in phase, the combined wave came out from the E-junction of this hybrid tee to the cryostat with a small loss due to the PCA of 2.5 dB. When out of phase, the combined wave escaped from the H-junction and was absorbed in the matched load, resulting in the maximum attenuation of about 20 dB. Fine control of the microwave power could also be achieved by adjusting the anode voltages of the sources.

The frequencies of the upstream and downstream microwaves were measured with two frequency counters[56] coupled to the main line after the PCAs using two attenuators in series with a total attenuation of 25 dB. The frequency was read by the computer via a GPIB interface. Small fractions of the microwave power were taken with the aid of splitters installed between these two pairs of attenuators and were fed to a thermocouple power meter via a microwave switch. This enabled microwave power calibration of the carbon resistors,[57] located inside the mixing chamber but outside the target cell, which were used as bolometers for the fine adjustment of the optimum input power, ranging from 0.8 W at the start of DNP to less than 100 mW at the maximum polarization.

To have the microwave sources out of the beam area they were connected to the cryostat via E-, V-, and K-band elements and 15 m of oversized X-band waveguides. Their transmission losses, including the junction parts, were about 6 dB and showed a rather flat frequency dependence. The thermal isolation in the microwave guides inside the cryostat was made with internally silvered thin-walled CuNi tubes of 4 mm diameter. The final connection to the cavity consisted of K-band waveguides soldered along the cavity wall and coupled to the inside via 7 equidistant slits, resulting in less than 10% of reflection loss.

Both target halves were located in a cylindrical multimode copper cavity of 210 mm diameter and 1700 mm length. This cavity was divided axially in two compartments by graphite coated copper baffles and copper reflectors to allow simultaneous operation with different microwave frequencies for both target halves. Inside the mixing chamber isolation of the two halves was obtained by using graphite coated Nomex honeycomb absorbers and fine copper mesh reflectors, designed to ensure free diffusion and convection in the dilute ^{3}He/^{4}He mixture. The microwave isolation was measured to be 20–30 dB in the 69–70 GHz band with empty cavities.

During the muon scattering experiments microwaves were continuously applied to achieve the highest possible polarization in the two target halves, except when the polarization directions were reversed by magnetic field rotation or during measurements of $A_\perp$ with transverse polarizations. Before the magnetic field rotations the system was brought in the Frozen Spin (FS) mode by switching the microwaves off. In this condition the target cooled rapidly to temperatures of about 50 mK, thus ensuring long relaxation times in a magnetic field as low as 0.5 T.

3.5. *The Nuclear Magnetic Resonance (NMR) electronics and probe design*

The nuclear spin polarization was measured with a continuous-wave NMR system, which was based on commercial "Liverpool" Q-meters[58] [41]. A block diagram of the NMR circuit is shown in Fig. 5. Due to the large dimensions of the target

[56] EIP 578.

[57] Speer 220 Ω.

[58] Ultra-Physics Ltd.

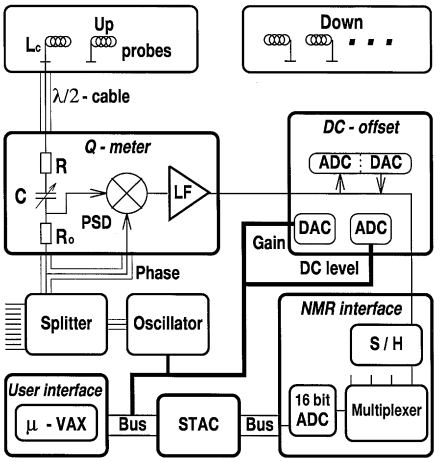

Fig. 5. Schematic outline of an NMR circuit.

cells, the NMR signal had to be probed simultaneously by up to ten NMR coils distributed along the target length. The radiofrequent (RF) susceptibility of the material was inductively coupled to the coils which were part of a series LCR circuit, tuned to the Larmor frequency of the nuclei under study. Section 4.1 describes the circuit analysis and the signal measurement in more detail. The probes inside the cryostat were connected to the Q-meters via tuned coaxial cables of half-integer wavelength (except for ^{14}N; see Section 4.4.3). The Q-meters were fed via a ten-way splitter by an RF synthesizer[59] of which the frequency was scanned in 400 frequency steps across the Larmor resonance. The RF voltage from the LCR circuit underwent an amplification of 42 dB by the Q-meter. A balanced ring modulator, acting as a phase sensitive detector (PSD) was used to select the real part of the output voltage. After an additional LF amplification by a factor of 30, the DC offset of the signal was subtracted by a circuit whose function was to provide a better dynamic range for the readout system. It worked by detecting the voltage at the lowest frequency of the baseline scan, obtained at a slightly altered magnetic field (see also Section 4.1), with a 12-bit ADC and then applying a DC voltage offset of the same value and opposite polarity with a DAC. This circuit provided also a DC level output to monitor the circuit stability. In the NMR interface the synchronous signal outputs were fed via sample-and-hold circuits in groups of four through three multiplexers into 16-bit ADCs. The digitized signals were then sent via an M68000 bus to a STAC[60] computer, where a desired number of frequency scans was averaged. The STAC also controlled other hardware components of the circuit such as the synthesizer and an oscilloscope [42]. Finally, the averaged signals were sent through a CAMAC bus connection to a μVAX computer providing the user interface, the data storage, and the analysis programs [43].

In addition to the requirements from the electronics point of view, the NMR coils had to fulfil various criteria arising from their use in our scattering experiment, so that an optimum design had to compromise on contradicting demands. The empty coil inductance L_c strongly affects the signal size and was chosen according to the nuclei under study, leading to 5 to 10 times higher inductance in the case of deuterons compared to the protons, where a large signal could result in non-linearities (Section 4.4.2). The small inductance of the proton coils leads to a smaller signal, in contradiction with the demand of full coverage of the target volume, while this was no problem for the deuterons. However, large embedded coils impair the dilution factor by adding background material.

The shape of the coils had to take into account both the desired RF field distribution and also the muon beam profile. The placement of the coils should be such that their highest sensitivity coincided with the maximum of the convolution of beam profile and target mass. The longitudinal arrangement had to balance between good coverage and tuning problems due to mutual coupling of coils which were too close to each other. Also the relative angle played an important role; perpendicular neighbouring coils showed increased distortions via dispersive contributions. The coils were made of cupronickel, which was available in the form of thin-walled tubes and had the advantages of a relatively high resistivity, which helped against

[59] PTS 250.

[60] Stand-Alone Camac module.

Table 4
Parameters of the various NMR coils, all made of $Cu_{0.7}Ni_{0.3}$, for the different measurements

Nucleus (Yr)	p (1993)	d (1994)	d (1995)	p (1996)	^{14}N (1996)
L_c (μH)	0.09	1.35	0.45	0.066	0.092
Q (at ω_0)	190	48	35	73	133
η_f	0.28	0.15	0.26	0.14	0.29
r_c (at ω_0) (Ω)	0.3	2.5	1.3	0.4	0.1
V_s (cm^3)	80	92	127	55	75
$\Delta\mathscr{S}$	0.40	0.62	0.38	0.75	0.59
Material	4 mm tube	3 mm strip	1 mm tube	3 mm tube	4 mm tube
Coating	(PTFE)	—	CH_2	FEP	—

Note: The deuteron coils of 1994 were originally designed for a cross-coil configuration and were not embedded in the material. L_c and r_c are the empty coil inductance and resistance, respectively. See the text for the other parameters.

superradiance (see Section 4.5), and a low resistivity dependence on temperature and magnetic field.

Coating of the coils by a layer of plastic material did help to avoid saturation effects due to large RF field strengths at the coil surface, especially for small tube diameters, and improved also the homogeneity of sampling in a large target. Of course, the coating material should not contain any free hydrogen in the case of the proton NMR, which otherwise would substantially contribute to the TE signal. For protons, coating also reduced the filling factor and thus the signal height.

The cables should disturb the measurement as little as possible. In the final set-up, we used 0.050 in. copper cables[61] inside the dilution chamber, connected via "home-made" vacuum feed-through's to copper clad stainless steel 0.085 in. cables[62] inside the evacuated part of the target holder. The connection outside the cryostat was made of 0.141 in. semi-rigid copper coax cables[63] without the usual PTFE insulation, because it was found to create circuit drift problems due to its phase transitions at 19°C and 30°C [44]. Special attention was paid to the NMR electronics and the temperature stability of the electronics and cables (to within 1°C) to obtain good measurements of weak signals, notably for the thermal equilibrium measurements of the deuterons at 1 K for calibration purposes [45].

Table 4 summarizes the characteristics of the various NMR coils used during the data taking. In Fig. 6 some typical coil shapes are shown. The filling factor η_f was calculated according to

$$\eta_f = \frac{\int_V x_m(\boldsymbol{r}) H_\perp^2(\boldsymbol{r})\,\mathrm{d}\boldsymbol{r}}{2\int_V H_1^2(\boldsymbol{r})\,\mathrm{d}\boldsymbol{r}} \tag{7}$$

where $H_\perp$ is the transverse component of the RF field with total strength $H_1 = (H_\parallel^2 + H_\perp^2)^{1/2}$, and x_m is the measured packing fraction of the material which has the value of ≈ 0.6 (see Table 2) in the volume occupied by the target material and zero elsewhere. The factor 2 in the denominator of Eq. (7) follows from the fact that only the component of the RF field rotating with the spins produces transverse magnetization while the counter-rotating component does not. The sampled volume V_s is defined as the volume giving rise to 95% of the NMR signal. The difference $\Delta\mathscr{S}$ in sampling the target material by the muon beam and by the NMR coils is given by

$$\Delta\mathscr{S} = \frac{1}{2}\int_{r<R} |c_{\mathrm{beam}} I_{\mathrm{beam}}(\boldsymbol{r}) - c_{\mathrm{NMR}} H_\perp^2(\boldsymbol{r})|\,\mathrm{d}\boldsymbol{r} \tag{8}$$

where R is the radius of the target container. The normalization constants c_{beam} and c_{NMR} are such that

$$c_{\mathrm{beam}}\int_{r<R} I_{\mathrm{beam}}(\boldsymbol{r})\,\mathrm{d}\boldsymbol{r} = c_{\mathrm{NMR}}\int_{r<R} H_\perp^2(\boldsymbol{r})\,\mathrm{d}\boldsymbol{r} = 1\ . \tag{9}$$

[61] Coaxitube DA50050 by Precision Tube Co.
[62] Coaxitube JN50085.
[63] Isocore IA–141NC by Rogers Co.

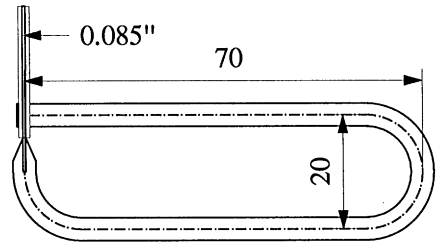

(a) proton (1993)

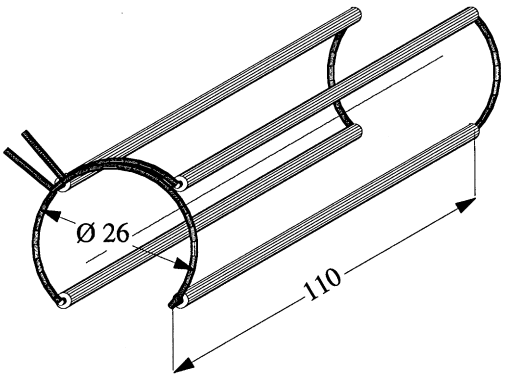

(b) deuteron (1995)

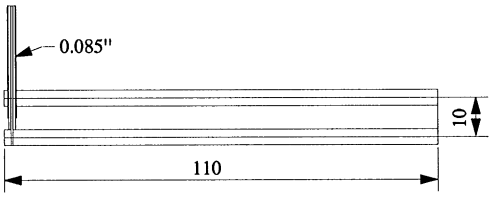

(c) proton and ^{14}N (1996)

Fig. 6. Several shapes of NMR coils used in the SMC polarized targets. The sizes are in mm, unless indicated in inches.

The muon beam profile $I_{\mathrm{beam}}(r)$ is in good approximation presented by a gaussian function with $\sigma = 12$ mm.

4. Target polarization and its measurement

The NMR system allowed us to monitor the proton and deuteron polarization in a semi-continuous way by determining the NMR signal area (integral method). Calibration runs were occasionally carried out with the target spins in thermal equilibrium at 1 K and with 2.5 T magnetic field. In the case of deuterated samples the polarization could also be determined from the asymmetric NMR lineshape due to quadrupole interaction. For the ammonia target also the ^{14}N polarization was determined. To determine the polarization accurately it is essential to analyse the NMR circuit in detail and to understand the various error sources. This is the subject of the following sections with the NMR results discussed separately for the three target materials.

4.1. Q-meter circuit analysis

The polarization of the target material is related to the NMR absorption by [21,46]

$$P = \frac{2\hbar I}{g^2\mu_{\mathrm{N}}^2 N\pi}\int_0^\infty \chi''(\omega)\frac{\omega_0}{\omega}\,\mathrm{d}\omega \equiv \frac{2\hbar I}{g^2\mu_{\mathrm{N}}^2 N\pi}\mathscr{A} \qquad (10)$$

where $\mathscr{A}$ is the "area" of the signal, μ_{N} is the nuclear magneton, I and g are the spin and g-factor of the nuclear species under consideration, and N is their number density in the sample. The quantity $\chi''(\omega)$ is the absorptive part of the complex nuclear susceptibility $\chi(\omega) = \chi'(\omega) - \mathrm{i}\chi''(\omega)$ where $\chi'(\omega)$ is the dispersive part. The absorption function for deuterons and protons in our target materials is non-zero for only about a 300 kHz range around the Larmor frequency ω_0. Thus, in order to calculate the polarization from Eq. (10), the absorption function only needs to be integrated over a small range of frequencies. The ratio ω_0/ω varies only slightly for protons and deuterons over this range and can be taken constant. The more complicated case of measuring the ^{14}N NMR signal, where the variation of ω_0/ω cannot be neglected, will be discussed in Section 4.4.3. Due to the target material the impedance Z_{c} of a coil varies as

$$Z_{\mathrm{c}} = r_{\mathrm{c}} + \mathrm{i}\omega L_{\mathrm{c}}(1 + \eta_{\mathrm{f}}\chi(\omega)) \qquad (11)$$

where L_{c} is the inductance of the empty coil, r_{c} is its resistance, and η_{f} is the filling factor defined in Eq. (7). The impedance is measured by the series-tuned Q-meter [41] which provides a complex voltage $V = V(\omega, \chi)$. The real part of V is selected by

the phase sensitive detector (PSD). The Q-meter is tuned so that the minimum of $V(\omega, 0)$ occurs at $\omega = \omega_0$.

The NMR signal is measured in two steps. Firstly, a "Q-curve" $V(\omega, \chi'' = 0)$ is measured by shifting B, and therefore the Larmor frequency, by a few per cent while keeping the RF scan in its nominal frequency range. In this case, $\chi''(\omega) = 0$ and $\chi'(\omega)$ is fairly constant for the entire frequency scan. Further in the paper we refer to this as the "baseline". The Q-curve $V(\omega, \chi'' = 0)$ represents the frequency response of the Q-meter. Secondly, the NMR signal $V(\omega, \chi)$ is measured on resonance by scanning the frequency at B_0. The two averaged signals are then subtracted, with the result that $\mathrm{Re}[V(\omega, \chi)] - \mathrm{Re}[V(\omega, \chi'' = 0)] \equiv S(\omega)$, which represents only the response of the Q-meter to the susceptibility function. In the following paragraphs, it will be shown that $S(\omega) \propto \chi''(\omega)$, from which it follows that the polarization is in very good approximation given by

$$P = \mathscr{K} \int_{\Delta\omega} S(\omega)\, \mathrm{d}\omega \tag{12}$$

where $\mathscr{K}$ is a constant involving both properties of the material and of the Q-meter. We determined $\mathscr{K}$ by making a thermal equilibrium (TE) calibration of the NMR system (Section 4.2.1).

A circuit diagram of the constant current series-tuned Q-meter is shown in Fig. 7; the circuit is driven by an RF source (synthesizer) of voltage

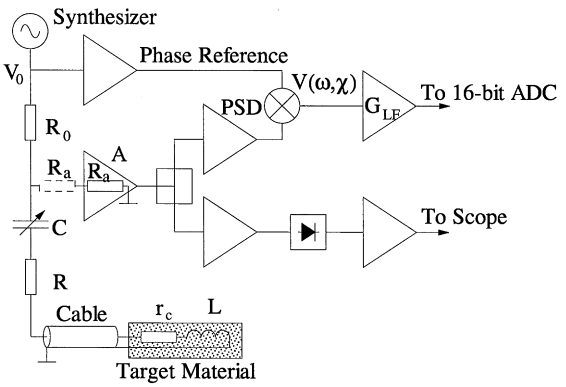

Fig. 7. Block diagram of the Q-meter circuit to measure the real part of the NMR signal.

Table 5
Typical circuit parameters for the proton, the deuteron, and the ^{14}N NMR

Parameter	Nucleus		
	p	d	^{14}N
ν_0 (at B_0) (MHz)	106.5	16.35	6.47
B_0 (T)	2.5	2.5	2.1
$\Delta\nu$ (kHz)	600	500	2×300
R_0 (Ω)	900	700	900
R (Ω)	33	10	10
R_a (Ω)	120	50	110
n	5	1	0.36

Note: The parameters ν_0, B_0, and n stand for the Larmor frequency, the corresponding magnetic field value, and the electrical length $\ell = n\lambda/2$ of the cable, respectively. For the explanation of the other symbols, see Fig. 7.

V_0 through a constant current feed resistance R_0. An amplifier with voltage gain A and input impedance R_a amplifies the signal. Typical circuit parameters are given in Table 5.

The NMR coil is connected to a Q-meter by a cable of impedance Z_{cable}, length ℓ and complex propagation constant $\gamma = \alpha + \mathrm{i}\beta$, where α is the attenuation factor and β is the phase constant. The total impedance of coil, cable, tuning capacitor C and damping resistor R (see Fig. 7), is given by [47,48]

$$Z(\omega, \chi) = R + \frac{1}{\mathrm{i}\omega C} + Z_{\mathrm{cable}} \frac{Z_{\mathrm{cable}} \tanh(\gamma\ell) + Z_{\mathrm{c}}}{Z_{\mathrm{cable}} + Z_{\mathrm{c}} \tanh(\gamma\ell)}\,. \tag{13}$$

The last term of this equation introduces nonlinearity if the susceptibility is large. The characteristic properties of the cable are its distributed resistance R_{cable}, inductance L_{cable} and capacitance C_{cable}. For a low-loss cable the quality factor $Q_{\mathrm{cable}} = \omega L_{\mathrm{cable}}/R_{\mathrm{cable}} \gg 1$ and the cable impedance is in good approximation given by

$$Z_{\mathrm{cable}} = Z_0 \sqrt{1 + \frac{R_{\mathrm{cable}}}{\mathrm{i}\omega L_{\mathrm{cable}}}} \approx Z_0 \sqrt{1 + \frac{1}{\mathrm{i}2Q_{\mathrm{cable}}}} \tag{14}$$

where $Z_0 = \sqrt{L_{\mathrm{cable}}/C_{\mathrm{cable}}}$ is the characteristic impedance of a lossless cable. With the electrical

length chosen to be an integer (n) times the half wavelength in the cable at the Larmor frequency, $\tanh(\gamma l)$ is real and equal to $\tanh(n\pi\alpha/\beta)$. The propagation constant is $\gamma = \{(R_{\text{cable}} + i\omega L_{\text{cable}})i\omega C_{\text{cable}}\}^{1/2}$, which gives for a low-loss cable in good approximation $\beta/\alpha \approx 2Q_{\text{cable}}$ and thus $\tanh(\gamma l) \approx \tanh(n\pi/2Q_{\text{cable}})$ at the Larmor frequency. For the 50 Ω cables used by SMC $\alpha \approx 0.024$ Np/m and $\beta \approx 3.16$ rad/m giving $Q_{\text{cable}} \approx 60$. Thus, by analysing the circuit, we see that the complex voltage at the output of the RF amplifier as a function of ω and χ is

$$V(\omega,\chi) = \frac{AV_0}{R_0}\,\frac{Z}{1+XZ} \tag{15}$$

where $X = R_0^{-1} + R_a^{-1}$ is the admittance due to the resistances R_0 and R_a. This equation can be inverted and solved for χ as a function of $\Delta V = V(\omega,\ \chi) - V(\omega,\ \chi'' = 0)$ which describes how the Q-meter affects the signal coming from the susceptibility. However, it is more enlightening to write the χ dependence of ΔV explicitly. To wit

$$\Delta V = \frac{D(\omega)\chi(\omega)}{1 + E(\omega)\chi(\omega)} \tag{16}$$

where $D(\omega)$ and $E(\omega)$ are complex, frequency-dependent coefficients [48]. From this explicit expression for ΔV as a function of χ'', we can expand Eq. (16) to low orders to investigate Q-meter effects. With $E(\omega)\chi(\omega) \ll 1$, the real part of ΔV is

$$\begin{aligned}\mathrm{Re}[\Delta V] \equiv S(\omega) = {} & \chi''\,\mathrm{Im}[D(\omega)] + \chi'\,\mathrm{Re}[D(\omega)] \\ & + (\chi''^2 - \chi'^2)\mathrm{Re}[D(\omega)E(\omega)] \\ & - 2\chi'\chi''\,\mathrm{Im}[D(\omega)E(\omega)] + \mathcal{O}(3)\ .\end{aligned} \tag{17}$$

The coefficients $D(\omega)$ and $D(\omega)E(\omega)$ calculated for a tuned circuit are shown in Fig. 8. The question is which terms in Eq. (17) contribute significantly to the integral of $S(\omega)$ in Eq. (12). $\mathrm{Re}[D(\omega)]$ is small and is zero at the Larmor frequency (see Fig. 8), and thus, gives a small contribution to the integral. With a sufficiently wide frequency scan, the third term of Eq. (17) gives a negligible contribution because of the Kramers–Kronig relation $\int_{-\infty}^{\infty}(\chi''^2(\omega) - \chi'^2(\omega))\,d\omega = 0$ [49,50] and the small variation of $\mathrm{Re}[D(\omega)E(\omega)]$ over the sweep range. The fourth term of Eq. (17) also produces only a small contribution to the integral because it is antisymmetric around the Larmor frequency. Thus, to a very good approximation the integration of $S(\omega)$ can be considered to depend only on $\mathrm{Im}[D(\omega)]$, that is

$$S(\omega) \propto \chi''(\omega)\mathrm{Im}[D(\omega)] \tag{18}$$

with $\mathrm{Im}[D(\omega)]$ in good approximation linear with ω and positive for the whole sweep range (Fig. 8). The "false asymmetry" of the deuteron NMR signals, discussed later in Section 4.2.3, is for a large part understood on the basis of the small deviation of $\mathrm{Im}[D(\omega)]$ from linearity with ω and higher-order terms given in Eq. (17), and is thus related to the properties of the electronics.[64]

For the large proton signals the higher-order effects can come into play. If the sweep width of the NMR system is not wide enough then the $\chi''^2 - \chi'^2$ term does not integrate to zero. The signal shape for high positive and negative polarizations becomes different (see Section 4.4.2).

4.2. The NMR of the deuterated butanol target

The deuteron has a spin 1 and a quadrupole moment which, together with the electric field gradient of the C–D and O–D bonds, shifts the energy levels depending on the angle between the magnetic field and the electric field gradient, and thus causes the characteristic shape of the NMR absorption signal (Figs. 9 and 10). In this case there are two ways to measure the polarization, namely (1) by the NMR signal area comparing it with a TE calibration (Section 4.2.1), or (2) by analysing the asymmetry of the NMR lineshape (Section 4.2.3). The TE method was used as the basic calibration and its result was cross-checked with the asymmetry method. The second method requires the polarization to be uniform, and it was used mainly to put limits to the non-uniformity of the deuteron polarization.

[64] There is a contribution to the false asymmetry from physical effects associated with the quadrupole broadening of spin-1 systems [51].

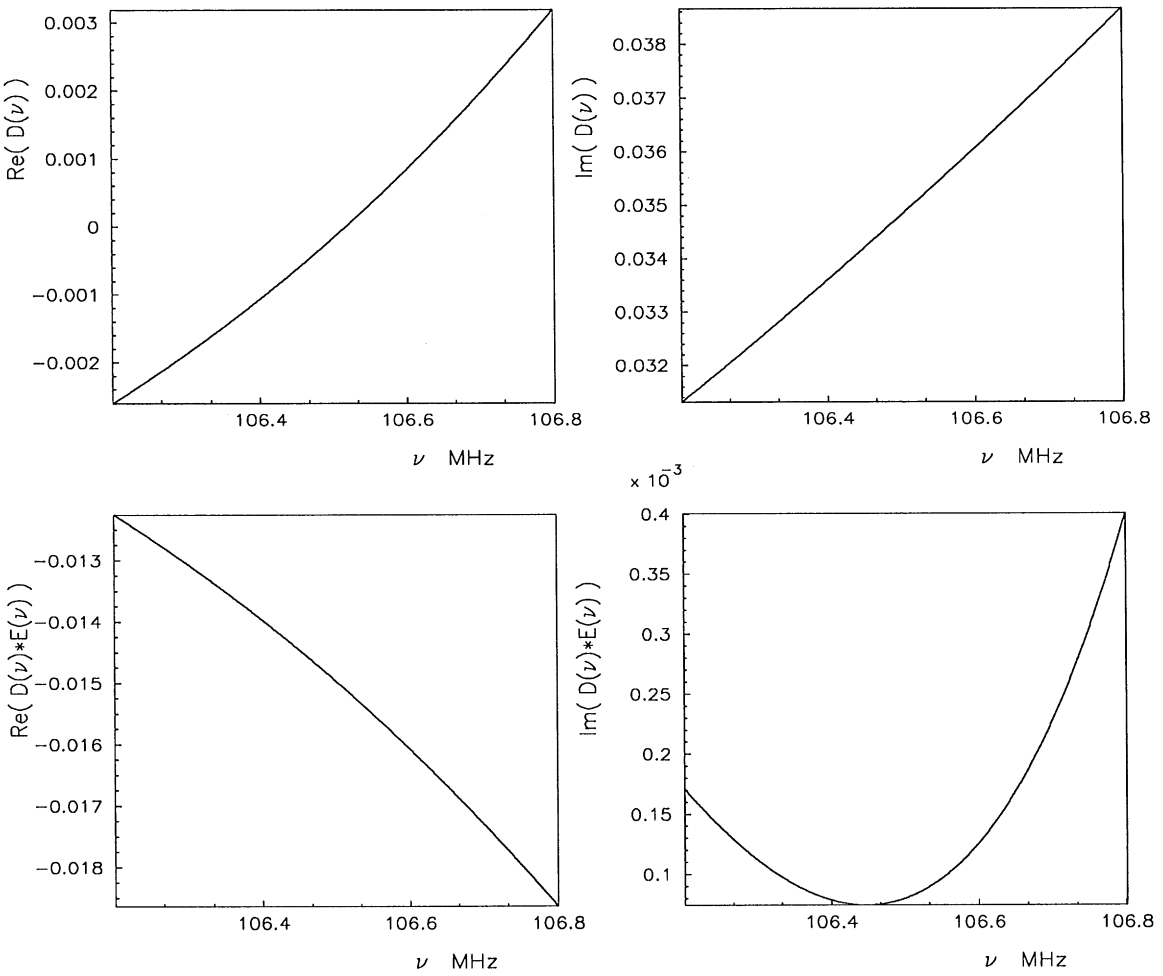

Fig. 8. The real and imaginary parts of the frequency dependent coefficients $D(\omega)$ and $D(\omega)E(\omega)$.

4.2.1. The thermal equilibrium calibration

The polarization P achieved by DNP was derived as the ratio of the enhanced absorption signal area to that of the thermal equilibrium signal

$$P = \frac{\int S_{\mathrm{enh}}(\omega)\, d\omega}{\int S_{\mathrm{TE}}(\omega)\, d\omega} \cdot P_{\mathrm{TE}} \tag{19}$$

where the TE polarization for a spin-1 particle at a given temperature and magnetic field could be calculated from the equation

$$P_{\mathrm{TE}} = \frac{4 \tanh(\hbar\omega_0/2kT)}{3 + \tanh^2(\hbar\omega_0/2kT)} \tag{20}$$

k being the Boltzmann constant and ω_0 the Larmor deuteron frequency.

The detection of the deuteron TE signal was difficult for two reasons: (1) at 1 K and 2.5 T the polarization was only 0.052%, and (2) it was broadened by the quadrupole interaction. Owing to the tiny TE signal of the deuteron, special care had to be taken to ensure sufficient signal-to-noise ratio and small system drifts. For a substantial noise reduction the signal was averaged over $n = 2000$ to 10 000 double sweeps, which reduced the statistical noise by a factor of $\sqrt{n}$. But due to the longer time needed to average the signals,

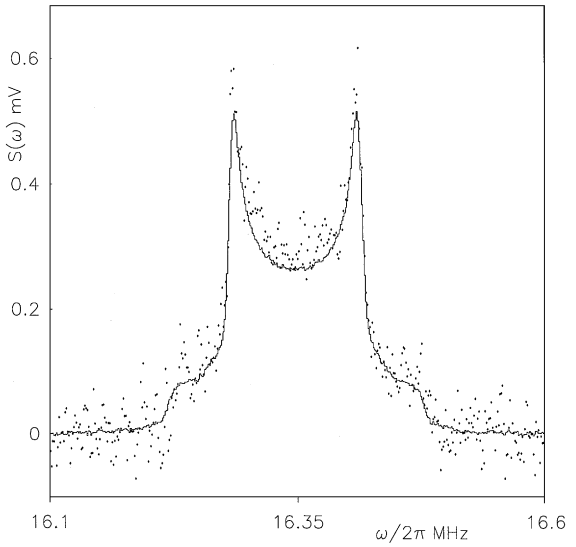

Fig. 9. The Q-meter signal S for deuteron polarization at thermal equilibrium (TE). The dots are the data points of a 2000 double sweep TE signal. The line is a super TE signal, which is the average of 380 of these TE signals, thus 760 000 double sweeps in total. The averaging reduces the noise sufficiently to allow a determination of the calibration constant $\mathscr{K}$ and, in addition, a reliable fit to the shape.

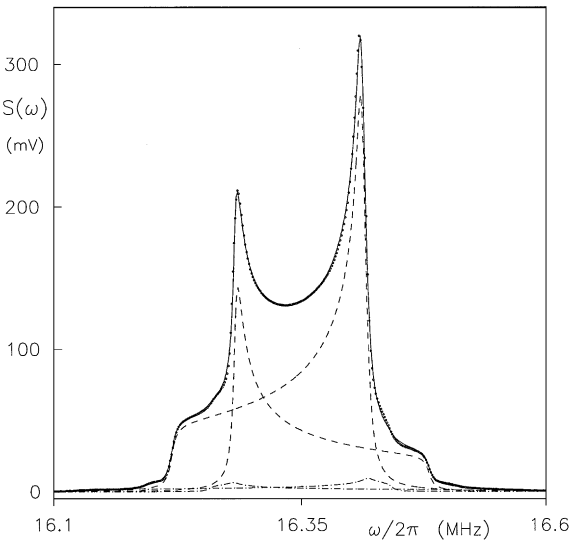

Fig. 10. The Q-meter signal for 44% enhanced deuteron polarization (dots) with the fitted curve (solid line). The dashed curves are the line shapes of the $m = 0 \leftrightarrow +1$ and $m = 0 \leftrightarrow -1$ transitions with quadrupole splitting and dipolar broadening. The two highest dashed curves are related to the C–D bonds; the two lowest dashed-dotted curves are related to the O–D bonds.

thermal drifts of the Q-meter parameters had an influence on the final accuracy, leading to an optimum between noise reduction by a large number of sweeps and short signal taking.

In addition, systematic tuning variations, mostly due to the magnetic field change necessary for measuring the Q-curve without absorption signal, altered the TE measurements [19]. To account for this, the Q-curve was taken alternatingly 5% above or below the Larmor frequency. Also a dependence of the TE coefficients on the magnetic field polarity, which was reversed for rotating the spin direction, was found. Up to 1000 TE signals were taken in the course of a few days which allowed additional systematic studies, e.g., of daily variations of the circuit parameters. The long-term stability of the NMR system was monitored by the RF level at the Q-meter output and, in addition, regularly cross-checked by TE calibrations. The long term instability was found to be 2% during the 1994 data taking, but improved to 0.5% in 1995. Fig. 9 shows a typical deuteron TE signal averaged 2000 times after subtraction of the Q-curve using a second-order polynomial fit to the absorption-free wings of the frequency scan.

In the following paragraphs we shall summarize the error analysis of the deuteron polarization measurements in 1995, while at some points we make a comparison with the measurements made in 1994.

4.2.1.1. Temperature measurement. TE calibrations were carried out in superfluid ^{4}He near 1 K in order to obtain a short polarization built-up time and good thermal uniformity and stability. TE signals were usually collected at two or more temperatures to have an additional cross-check of systematic errors in the temperature measurement. For an accurate temperature determination we used liquid ^{3}He in a separate small bulb mounted inside the mixing chamber and measured the ^{3}He vapour pressure by means of a high precision capacitive pressure gauge.[65] Table 6 summarizes the uncertainties of this temperature measurement and its stability for the 1995 data taking.

[65] MKS Baratron 270B.

Table 6
Errors of the TE temperature measurement of the 1995 deuteron run

Error sources; TE temperature	$\lvert\Delta T/T\rvert$ (%)
Baratron gauge head accuracy	0.08
Electronic linearity	0.005
Gain factor uncertainty	0.2
AD-conversion	0.012
Reference vacuum	0.2
ITS-90 temperature scale	0.1
Thermomolecular effect	0.1
Instability	0.2
Spatial uniformity	0.003
Total error	0.38

4.2.1.2. NMR system noise and drift. We have introduced a new technique to detect and monitor very small changes in the NMR system based on two considerations:

(1) The outermost edges of the frequency scan are the most sensitive parts of the Q-curve for detecting small changes of the Q-meter's resonance frequency (i.e., the minimum of the baseline), which cannot be found when the NMR signal is in place. We used the difference of the first and the last channel content, called tuning, as a monitor for frequency changes. The change in the tuning is proportional to $\Delta\omega$, which was found to be proportional to ΔP.
(2) The sum of the first and the last channel gave us a direct relative measurement of the DC-level, i.e., the change in the quality factor Q of the system, which is (for small changes) also proportional to ΔP. To make this method to work, we had to disable the automatic DC-subtraction by the DC-offset card after storing once the right values to bring the parabola in the mid-range of the ADC.

The contribution of the thermal drift of the circuit could not be separated from the other tuning changes. The origin of the drift was mostly inside the refrigerator and due to temperature changes in the mK range. In addition, we observed daily variations of the parameters which could be traced back to temperature variations of the NMR rack and of the $\lambda/2$-cables [44]. The averaging over both baseline measurements with the field shifted up and down by a small percentage had the additional advantage of reducing greatly the system drift by subtracting the mean Q-curve before and after each signal. The period of the drift was several hours, so that through this method the residual drift became very small.

The relative statistical error of the final TE coefficient was calculated by $\sigma = \mathrm{RMS}/\sqrt{n}$ and contained also the spreading due to noise. A further analysis of the TE data showed that this $1/\sqrt{n}$ dependence was justified and that a shift of half the signal areas by a fixed amount (e.g., due to the magnetic field) did not harm the accuracy of the mean value of the TE signal.

4.2.1.3. Long-term tuning changes. Another systematic error was due to the contribution from long-term tuning changes, which caused signal area changes since the response function of a Q-meter is frequency dependent. In order to determine the magnitude of this effect on the polarization reading, the tuning was offset by shifting the Larmor frequency and the integration window at the same time in the frozen spin mode. An additional error can be assumed for the DC level change between calibrations. This change was translated into a relative percentage of polarization change by assuming linear scaling with the Q-value, i.e., the DC-level.

4.2.1.4. Field polarity effect. It was observed that the calibration constants showed a small dependence on the polarity of the magnetic field. We did not apply polarity dependent TE coefficients as for protons in 1993, even when the effect became more pronounced due to the better TE signal quality. It turned out that this effect was hard to compensate for two reasons: Firstly, the polarity effect was entangled with the larger day and night variations of the system parameters. Especially for a short calibration run the unbalanced times led to false differences in the coefficients. Secondly, the polarity effect turned out to be temperature dependent.

The average field polarity effect (see Fig. 11) was taken into account by a general correction to the averaged polarization upstream and downstream by adding half the jump to the lower polarization

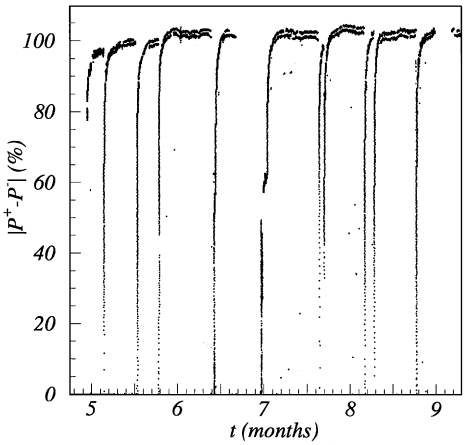

Fig. 11. Difference $|P^+ - P^-|$ between the polarizations of the target cells during the 1995 deuteron g_1^d measurement. When the magnetic field is reversed the polarization difference alters slightly. This field polarity effect is clearly visible in the flat regions.

and subtracting the same amount from the higher one. It turned out that the mean values for both temperature regimes were quite the same. For this systematic error we assumed, conservatively, 100% of that correction.

4.2.1.5. TE relaxation time. Because of the finite relaxation time τ of the polarization there can be a systematic effect on the TE-calibration due to the fact that the baseline had been taken at a 5% higher or lower field. This could lead to an up to 5% larger or smaller TE signal area relaxing exponentially to the original value when the field was back at its nominal value. The possible effect on the coefficients was largely diminished by the fact that we took the baselines alternatingly at higher and lower fields. This procedure should average the effect to zero, but would broaden the distribution. In addition, we waited several minutes after reaching 2.5 T again before taking the first signal. The relaxation time was measured with an enhanced signal at 1 K to be $\tau = 2.0 \pm 0.2$ min. From this number we could estimate that this broadening was negligible small.

4.2.1.6. TE off-centering. A small contribution to the error was associated with the mean centering of the TE-signals. There was a polarity dependent bias arising, because the normal centering algorithm did not work well with noisy signals. However, the TE-supersignals (i.e., an average of about 100 TE signals) showed the centres very well. From the study of the distribution of the centres we deduced the systematic error due to integration, and due to the Q-meter response function.

The magnitudes of the main error sources in the determination of the TE signal area are shown in Table 7. The TE coefficients were averaged over the two baseline fields and over the field polarities.

4.2.2. The enhanced signals

As the enhanced signals were much larger than the TE signals, some of the error sources mentioned above for the TE signals were negligible, especially noise. However, system drifts while irradiating the target with microwaves, and lineshape changes due to the dispersive component or the cross-talk between the coils were sources of systematic errors. A gain variation was observed between the TE calibration measurement and the low temperature measurements when the dilution refrigerator was operating. This was because the parameters of the NMR circuit inside the cryostat were slightly temperature dependent. Some of the major systematic changes of the signal area arose when the transition was made from dynamic nuclear polarization (DNP) to the frozen spin (FS) mode. Here follows a treatment of error sources for enhanced signals.

4.2.2.1. Tuning and DC level change between the TE and dilution modes. With some of the circuit parameters temperature sensitive, the largest change

Table 7
Summary of the deuteron TE signal area errors in 1995

Error sources; TE signal	$\lvert\Delta P/P\rvert$ (%)
Calibration statistics	0.20
Long-term tuning change	0.32
Field polarity effect	0.62
Long term DC level change	0.32
TE relaxation	0.05
TE centering	0.24
Total error (TE)	0.83

*Note: For the field polarity effect the residual error after correction is shown.

was observed between the TE-mode (^{4}He at 1 K) and the dilution mode ($T < 300$ mK). Using the tuning and DC-level information described above, we could monitor the signal area changes.

4.2.2.2. Tuning change between DNP and FS modes. A change in signal area due to microwave heating was observed in 1994 when large-inductance NMR coils were employed. It led to a $\leqslant 2\%$ relative change in the signal area when going from the FS mode to the DNP mode. It could be partly compensated by raising the temperature of the mixing chamber by using an electric heater, while the baselines in the FS mode were taken. The origin of this effect is still unknown but has possibly to do with the temperature-dependent resistivity of the copper-clad cryogenic coaxial cables of the NMR probes. By reducing the inductance of the coils for the 1995 run this effect largely diminished. The effect of the microwave heating on the signal areas was found to be polarity dependent.

4.2.2.3. Tuning change due to RF level variations. Sudden RF-level jumps, on the order of 1%, were visible. The origin of these jumps is not known; the RF source itself or its transmission line are not ruled out.

4.2.2.4. Cross-talk between the target cells. The RF cross-talk between the target cells was measured by polarizing only one cell and observing the signals in the other. In 1994 a large dispersive signal was seen, which caused concern because of the fact that during the TE calibration both cells were positively polarized while during the physics run the polarization was always opposite, so that the effect did not cancel. We found that most of the cross-talk signal was transmitted via the coaxial cables, passing from one cell to another. Thus, the distance between the NMR coils and the coaxial cables played a vital role and led to our decision to return to embedded coils. The cross-coupling was further reduced by improving the RF grounding of the microwave stopper and by dividing the ^{3}He inlet tube in two sections, which were not electrically connected.

4.2.2.5. Dispersive signal. Our theoretical understanding of the NMR circuit improved during the course of the experiments, leading to detailed descriptions and predictions for the system behaviour, including the response functions of both the absorptive and the dispersive parts of the signal, and the higher order non-linear signal distortions [48,52,53]. In the case of the TE signal the dispersive part was fully antisymmetric[66] with respect to the Larmor frequency and should give no contribution to the polarization error. But in the enhanced case the two peaks of the deuteron signal became more and more unequal in height which was also reflected in the dispersive part. The Kramers–Kronig relation guaranteed that the total integral was zero even in this case but, due to our limited frequency scan, deviations might occur. In particular, this happened for the case when there was a tuning difference between Larmor frequency and NMR circuit. Theoretical estimates of this effect were of the order of 1–2% in 1994, while in 1995 this effect was very small.

There was a small effect due to the fact that we normally took the baselines at a 5% reduced magnetic field. A substantial amount of dispersion existed at the baseline field, as the relative width of the absorption signal was already 1.2% and the dispersive part was much broader. The effect was enhanced by the large difference between the Larmor and the circuit resonance frequencies when the field was changed, which led to a large dispersive signal due to the response function. This effect was quantified by comparing the baselines taken below and above the nominal field. In 1994 its contribution was $|\Delta P/P| = 0.3\%$ but in 1995 it was negligible.

4.2.2.6. NMR depolarization. The polarization loss of the large coils due to NMR turned out to be only 0.025%/h, using the "economy mode" for the measurement, when the NMR signals were taken only every 5–10 min. Assuming a linear decay of the polarization and taking into account that we stayed in FS mode for 24 h at most during data taking, we could derive an upper limit for the resulting error.

[66] The corresponding response function is also antisymmetric, but with respect to the resonance frequency of the circuit, so the resulting contribution is symmetric if the tuning is correct.

Another concern regarding the NMR depolarization dealt with the possible bias of the polarization value due to the balance between the build-up of the polarization via DNP with increasing characteristic time constants[67] and the continuous destruction of the polarization through the RF. To find this out, the target was polarized for several hours without NMR measurements starting at very high polarizations with optimum frequency and power settings. If the polarization close to the NMR coil wires had been substantially smaller before, due to NMR depolarization, then it should have built up during that time. Thereafter we switched off the microwaves and went to FS mode, freezing in the polarization. After some time, we enabled the NMR measurement again and looked for the decay of the signal with time, during which the closest beads would depolarize back to the "saturated" value. The observed decay constants agreed with the number stated above. However, we could deduce an upper limit for this bias, assuming that the "recovery" of the former state took roughly the same time as during the build-up without saturation (around 3 h). See Section 4.5 for more details about the effect of NMR on the polarization.

4.2.2.7. Integration error. After subtraction of the baseline, the signals showed a residual baseline, which was treated with a second (or third) order polynomial fit to the wings. When both the signal and the baseline were taken in FS mode, the residual baseline of the enhanced signals turned out to be close to a straight line, and the error involved in the subtraction of the wing-fit was minimal. But in the case of DNP, the temperature difference, that occurs between the times that the baseline and signal were taken, caused a tilt of the raw signals due to a non-negligible residual baseline. This effect was mostly due to tuning changes of the microwave-heated circuit as described before. However, by a careful analysis of the tuning change, we found that the effect arose from two different origins: the tuning change itself and the error on the fit of the residual baseline.

4.2.2.8. LF gain variation. The temperature dependence of the LF amplification was measured in order to evaluate the error due to variations of the ambient temperature.

4.2.2.9. Homogeneity. In the error of the averaged polarization value the homogeneity throughout both of the target cells played a role. The longitudinal homogeneity was less important due to the "smearing" in the vertex resolution and the "averaging" by the beam. The standard deviations of the distributions of the polarization values measured in the individual NMR coils were small, indicating no significant longitudinal inhomogeneity.

However, a possible large radial dependence of the polarization could cause serious systematic problems. In order to determine whether a sizable radial gradient of polarization exists, two small coils were mounted in one of the target cells. One of these coils was on the axis and the other close to the sample edge. The radial dependence of the polarization measured by these coils revealed a small effect of the order of 2% which had opposite signs for the two polarization directions. We noted that the ratio of the polarizations in the two small coils deviated more from unity for low polarizations than for high polarizations. This indicated that the polarization difference we observed was real, and not just an artifact of the TE coefficients. In the 1995 run the NMR coils sampled the central area of the target[68] where the beam went through. Therefore, the small radial dependence made only a minor contribution to the systematic error.

4.2.2.10. Polarization averaged over space and time. The statistical part of the error should decrease as $1/\sqrt{n}$ by the averaging over the number of coils, n. Unfortunately, the leading uncertainties were of systematic nature. Usually there were several polarization measurements for each physics "run", and these readings were averaged over the run. The standard deviations of these distributions were normally well below 1%, except for the periods soon after polarization reversals by DNP.

[67] The typical time constants in the TE mode were a few minutes and thus much shorter than in the dilution mode; therefore, this bias was not included in the calibration constants.

[68] The NMR coil wires were placed at a radius of 14 mm to minimize the sampling difference between the beam and the coil.

Table 8
Summary of the deuteron enhanced signal errors in 1995

Error sources; enhanced signal	$\lvert\Delta P/P\rvert$ (%)
Tuning change TE/dilution mode	0.5
DC level change TE/dilution mode	1.0
Tuning change DNP/FS mode	0.5
RF level variations	1.0
Cross-talk	0.4
Dispersion	0.1
NMR depolarization	0.5
Integration	0.4
LF gain variations	0.2
Radial gradient/homogeneity	0.1
Total error enhanced signal	1.8

No additional error was attached to this spread as it should cancel out for a large number of runs. The normalized inverse errors on the TE calibration coefficients were used as weights in the calculation of average polarization in each cell.

4.2.2.11. Summary. The main error sources and their contributions to the enhanced signal error are shown in Table 8. The final error of the polarization measurement in 1995 was estimated from Tables 6–8 to be $|\Delta P/P| = 2.0\%$.

4.2.3. Polarization determination by the asymmetry method

In this section we will use a theoretical model of the deuteron line shape [51,54], which is fitted to the experimental line shape to extract the polarization P_{AS}. In our representation of the absorption function we assume that the spin temperature of the system is uniform throughout the sampling volume of the NMR coils. Numerical methods have been used in previous works by Hamada et al. [55], by Wait et al. [56], and by Sperisen [57], to fit theoretical line shapes to deuteron signals in hydrocarbon materials.

First order quadrupole splitting in the electric field gradients, which can be asymmetric about the bond axes, is considered. In our line shape model for deuterated butanol, the local electric field gradients of the C–D and the O–D bonds coupled to the quadrupole moments of the deuterons cause an asymmetric shift of the energy levels into two overlapping absorption lines. The energy levels of such a spin-1 system are written as [22,23]

$$E_m = -\hbar\omega_d m + \hbar\omega_q\{3\cos^2(\theta) - 1 + \eta\sin^2(\theta)\cos(2\phi)\}(3m^2 - 2)\ . \quad (21)$$

The first term represents the magnetic splitting with frequency ω_d and the second term the quadrupole interaction with θ being the polar angle between the axis given by the C–D or O–D bond and the static magnetic field $\boldsymbol{B}_0$, and $m\,(=-1,0,1)$ the spin magnetic quantum number. The strength of the quadrupole interaction is described by $\hbar\omega_q = eq\,eQ/8$ where eq is the magnitude of the electric field gradient along the bond direction and eQ is the electric quadrupole moment of the deuteron. The azimuthal angle ϕ and parameter η are necessary for describing bonds in which the electric field gradient is not symmetric about the bond axis [22,58].

In the analysis of the quadrupole line shape the dipolar broadening is taken into account as a Lorentzian function with broadening parameter $\sigma = 3\omega_q A$. The absorption function can be written as

$$\chi''(r,R) \propto \left(\frac{1}{\omega_q}\right)\left\{\left[\frac{r^2 - r^{1-3\vartheta R}}{r^2 + r^{1-3\vartheta R} + 1}\right]F_+(R,A,\eta) + \left[\frac{r^{1+3\vartheta R} - 1}{r^2 + r^{1+3\vartheta R} + 1}\right]F_-(R,A,\eta)\right\}\ . \quad (22)$$

$F_\pm(R,A,\eta)$ are line shape functions [51,54] related to the $m = 0 \leftrightarrow +1$ and $m = -1 \leftrightarrow 0$ NMR transitions for which $R = (\omega - \omega_d)/3\omega_q$ varies over the $-2 < R < [1 - \eta\cos 2\phi]$ and $-[1 - \eta\cos 2\phi] < R < 2$ ranges, respectively. These line shape functions have peaks at $R = \pm[1 - \eta\cos 2\phi]$ if dipolar broadening can be neglected. In Eq. (22) $\vartheta = \omega_q/\omega_d$ and $r = e^{\beta\hbar\omega_d}$, with $\beta = 1/kT_s$, is the asymmetry parameter which is basically the intensity ratio of the two transitions. The line shapes of the two NMR transitions can be seen in Fig. 10, in which the total NMR line shape is decomposed in its components. The two strongest lines are related to C–D bonds, the other two are due to O–D bonds. Dipolar broadening is included

in these line shapes, which have a peak and a shoulder. Comparing the "peak-to-peak" width to the "shoulder-to-shoulder" width provides information about η. The asymmetry parameter r can be used to express the polarization P_{AS} in the spin temperature T_s; that is, up to second order in ω_q

$$P_{AS} = \frac{r^2 - 1}{r^2 + 1 + r}\left\{1 - \frac{6}{5}\frac{\vartheta^2 r \ln^2(r)}{r^2 + r + 1}\right\} . \quad (23)$$

For deuterated butanol material in a 2.5 T field $\vartheta \approx 10^{-3}$; the absorption function can in good approximation be written as

$$\chi''(r, R) \propto \left(\frac{1}{\omega_q}\right)\left(\frac{r-1}{r}\right) \times \{rF_+(R, A, \eta) + F_-(R, A, \eta)\} . \quad (24)$$

The quadrupole coupling ω_q (thus R) differs between the O–D and C–D bonds. Their relative amounts are represented by a constant factor K. Contributions from D_2O and the EDBA complex are included. It is assumed that the polarization of the deuterons is the same whether they are attached to carbon or oxygen and that the dipolar broadening parameter σ is the same for the two bonds. Inspection of the experimental deuteron signal in Fig. 10 shows that $\eta = 0$ can be accepted for the C–D bond since the "shoulder-to-shoulder" width is twice as large as the "peak-to-peak width". To wit, the total absorption function for deuterated butanol is

$$\chi''_{but}(r, R, \sigma, \eta) = (1 - K)\chi''(r, \sigma, R^{car}, \eta = 0) + K\chi''(r, \sigma, R^{oxy}, \eta) \quad (25)$$

where either of Eq. (22) or Eq. (24) can be used to represent χ'' for analysing deuteron signals.

The NMR signals with the Q-curves subtracted can be written as

$$S(\omega) = C\chi''_{but}(\omega) + a_0 + a_1\omega + a_2\omega^2 + a_3\omega^3 . \quad (26)$$

The a_i-terms are introduced to remove a residual background by fitting this third-order polynomial to the wings of the NMR signal. The first coefficient of Eq. (26) can be expressed as

$$C = C_0\{1 + \tfrac{1}{2}\xi(1 + R)\} \quad (27)$$

in which C_0 represents the constant gain factor of a Q-meter and ξ is the false asymmetry parameter. The equation is written in this manner so that ξ is the difference in gain between the two peaks in the signal.

4.2.3.1. Results of the signal analysis. The total expression for the NMR signal that was fitted to the data contains 13 fitting parameters. The absorption function was described by the 8 parameters C_0, r, ω_d, σ, ω_q^C, ω_q^O, plus η for the O–D bond only, and K for the ratio of the O–D and C–D contributions. In addition, the instrumentation required 5 fitting parameters; ξ from the false asymmetry, and a_0 to a_3 from the residual background. Fig. 10 shows an example of such a fit to the enhanced deuteron signal at 44% polarization.

In Fig. 12, P_{AS} is plotted versus P_{AR}, the polarization determined by the integral method, for both signs of polarization. For polarizations above 30%, the agreement between the two methods is within the $\pm 3.0\%$ relative error. The determination of the polarization from the asymmetry method assumes that the polarization is uniform throughout the sampling volume of the coil since one temperature T_s (i.e., β) is used to describe the system. The good agreement between the two methods at the highest polarizations supports this assumption. At the lower polarizations the two methods diverge slightly which is an indication that at these values the polarization is not uniform during the early

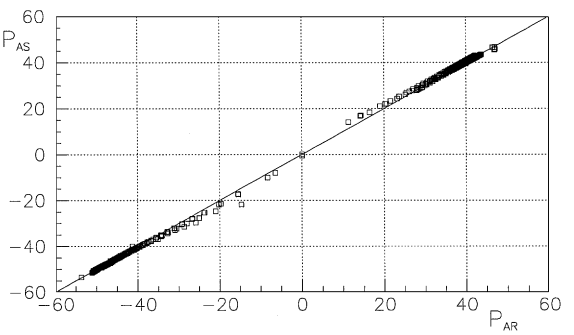

Fig. 12. A plot of P_{AS} versus P_{AR} with the $P_{AS} = P_{AR}$ line superimposed for deuterated butanol. The data represent signals collected at different times during a period of several months. The deviation at low polarization may be a sign of non-uniform polarization occurring during the DNP process.

stage of the DNP process in which the rate of increase is large.

The asymmetry method was not used as a substitution for the TE calibration in the determination of the polarization, because a good measurement of the area of the TE signals was needed anyway for adjusting ξ in the asymmetry method. The asymmetry method allows confirmation of the polarization values and tells whether the polarization throughout the sampling volume of the coil is homogeneous.

4.3. The proton NMR of the butanol target

The TE polarization of the proton, $P_{TE} = \tanh(\hbar\omega/kT)$, is about five times higher than that of the deuteron. In addition, the NMR signal is narrow due to the absence of quadrupolar broadening. Thus the main error sources in the proton polarization measurement are different from those discussed above for the deuteron target. The effects of noise and drifts are greatly reduced owing to the large signals but this introduces also a new problem; that is, the response of the Q-meter is linear only in the limit of small signal height compared to the Q-curve. Here we shall present the main error sources and corrections which apply to the butanol target in 1993 [59].

4.3.1. Temperature measurement errors

In the 1993 run, the capillary of the ^{3}He vapour pressure manometer was blocked during the TE measurements and alternative ways for temperature measurement had to be relied upon for the butanol target. These were resistance thermometry using calibrated Speer and RuO thermometers, read out by 4-wire AC resistance bridges, and vapour pressure measurements of ^{4}He in the still.

To improve the systematic uncertainties of the calibration, the still heater was used to raise the calibration temperature in small steps around 1 K. Table 9 gives an overview of the main error sources in the temperature measurement. The leading error originated from the readout noise of the capacitive pressure gauge, especially at the lowest temperatures (the vapour pressure of ^{4}He is about 100 times smaller than that of ^{3}He). Substantial errors arose due to extrapolation of the ITS-90 temperature scale below 1.25 K[69] and due to the thermomolecular effect. The small instability during the TE signal averaging (of about 4 min) was found to contribute as well. Other errors related to the pressure gauge were a bias due to the reference vacuum and an observed inconsistency of the various ranges.

Table 9
Main error sources of the TE temperature measurement of the 1993 proton run

T (K):	1.0	1.2	1.4	1.6
Error sources; temperature	ΔT (mK)			
Range	3.0	3.0	3.0	3.0
Reference vacuum	3.0	1.0	0.3	0.1
ITS-90	5.0	2.5	1.0	1.0
Thermomolecular effect	3.0	1.0	0.2	0.1
ADC	1.0	0.5	0.2	0.1
Film creep	0.4	0.2	0.1	0.1
^{3}He contamination	0.3	0.3	0.3	0.3
Instability	3.0	3.0	3.0	3.0
Noise	8.0	4.0	2.0	2.0
Total error (mK)	11	7	5	6
$\lvert\Delta T/T\rvert$ (%)	1.1	0.6	0.4	0.4

Of minor influence were the ADC resolution of the pressure reading, the film creep of superfluid ^{4}He inside the manometer tube, and the contamination of ^{4}He with ^{3}He. Other possible sources, like pressure differences due to still pumping, field dependencies, or self-heating of the resistance sensors, were evaluated to be negligible. All in all, these errors in the temperature determination resulted in an overall error of the polarization $|\Delta P_T/P| = 0.8\%$.

4.3.2. TE signal area errors

The averaging was done over $n = 2000$ double sweeps, which reduced the noise by $\sqrt{n}$, but the long measuring time increased the influence of thermal drifts in the Q-meter parameters. In Table 10 we list the main uncertainties of the TE

[69] Below 1.25 K the ITS-90 scale is based only on ^{3}He vapour pressure.

Table 10
Errors in the TE signal area measurement of the 1993 proton run

Error sources; TE signal	$\lvert\Delta P/P\rvert$ %
Polarity	0.6
Magnetoresistance	0.5
Background	0.4
Long term drift	0.4
Q-curve jumps	0.3
Noise	0.3
Relaxation	0.2
Short term drift	0.1
Total error TE signal	1.1

signal which result in a total error of the TE signal area of $\pm$ 1.1%.

Note that the noise was the only statistical error source, while all the others were systematic. For two of the main error sources, namely for the proton background signal of the empty target containers and for a field polarity effect on the calibration coefficients, corrections were applied. The background NMR signal was found to be of the order of 1% of the TE signal size but with a relatively large uncertainty. The influence of the field polarity on the signal areas was possibly caused by the stray field on the 10-way RF splitter containing ferrite elements.

Other main sources of uncertainty in the TE signal were the slight tuning changes at the 1.5% higher baseline field due to magnetoresistance of the coils and cables inside the cryostat, drifts of the Q-meter circuits, noise, and observed small irregular jumps in the Q-curves, for which no satisfactory explanation could be given so far. There is also a small contribution due to the change in the TE polarization caused by the baseline taking at a different field, together with the finite relaxation time on the order of a few minutes.

4.3.3. The enhanced signal errors

One of the main problems in the polarization measurement arose from the large modulation depth of the strongly enhanced signals, i.e., the signal height relative to the RF-level at the minimum of the Q-curve. It exceeded 60% for the negative signal, which led to a non-linear distortion of the line shapes and, thus, to a wrong estimation of the signal area. The correction to be made on the polarizations due to our simulation of the Q-meter circuit was on the order of 5% with a residual uncertainty of up to 0.9%. The correction was dealt with in detail in Ref. [53].

A correction was also necessary for the signal shift caused by the internal magnetization of the material. Other error sources were the deviation from linearity of the phase sensitive detector (PSD), sudden tuning changes, and a possible contribution from the hyperfine-broadened signal from the protons in the EHBA–Cr(V) complex, which could not be measured. In Table 11 the leading error sources of the enhanced signals are summarized for the two sweep widths of 400 and 600 kHz during the 1993 run, adding to an overall error of 1.2% and 1.0%, respectively. The LF amplifier gain ratio between the TE and enhanced signal turned out to introduce an error on the order of 0.5%.

The polarization values, given by the individual coils, were averaged for both target cells and over the time of one data run (typically 30 min). After corrections the largest differences within each cell were below 3%. To probe for a possible radial inhomogeneity, two small coils were installed in the upstream target, one in the centre and the other about 1 cm from the centre. The readings from these coils differed only slightly.

Table 12 gives an overview of applied corrections to the proton polarization values and the

Table 11
Errors of the enhanced signal area estimation of the 1993 proton run

Sweep width (kHz):	400	600
Error sources; enhanced signal	$\lvert\Delta P/P\rvert$ (%)	
Non-linearity	0.90	0.60
Non-linearity of PSD	0.60	0.60
Off-centering	0.50	0.40
EHBA signal	0.15	0.15
Drift	0.30	0.15
Tuning jumps	0.50	0.50
Total error enhanced signal	1.2	1.0

Table 12
Corrections applied to the raw values and their residual errors of the polarization during the proton run in 1993

Correction	Magnitude (%)	Residual Error (%)
Background	1.0	0.4
Polarity	2.0	0.6
LF gain	2.0	0.5
Off-centering	0.6	0.5
Non-linearity	4.0	0.8
Combined error		1.3

corresponding errors. The overall error of both target halves over the whole run, including the small inhomogeneity observed by the different probes, turned out to be

$$|\Delta P_{\mathrm{tot}}/P| = 3.0\% \ .$$

4.4. The NMR of the ammonia target

4.4.1. Measurement of proton polarization

In ammonia, the protons are arranged in triangular configurations, resulting in an asymmetric NMR line shape at high polarizations. We developed an approximate model for the line shape in order to estimate the correction due to non-linear response of the Q-meter. To minimize the correction, the filling factor of the proton coils was reduced by an FEP coating. One coil (see the N/p-coil in Fig. 6(c)) was left unwrapped and it was used to measure both the proton and the ^{14}N polarization. Another reason to reduce the filling factor was superradiance which was for this sample even more pronounced than in the butanol target. In an extreme case the polarization changed by superradiance from -88% to $+28\%$ locally around the NMR coil. To overcome this effect, small-inductance coils were used to avoid that coil resonances lie at proton Larmor frequencies which were swept through during the rotation procedure. However, it turned out that superradiance could be suppressed by making the solenoid field inhomogeneous during ramping by reversing the trim coil currents as in 1993 with the butanol target. Here we shall summarize the error analysis for the proton polarization measurement in 1996.

The thermal equilibrium (TE) signal areas were obtained at about 1 K by first shifting the field by $\pm 1.5\%$ and then recording the Q-meter resonance curve. The signal was measured by averaging 2000 double frequency sweeps over the 600 kHz range. The proton relaxation time was measured to be about 20 min at 1 K, but by performing the field shifts symmetrically the error due to relaxation cancelled out.

Table 13
Summary of TE calibration errors

Error sources; proton TE signal	$\lvert\Delta P/P\rvert$ (%)	
	N/p-coil	p-coils
Temperature; statistical	0.1	0.1
Temperature; measurement	0.3	0.1
TE area; statistical	0.4	0.4
TE area; drift	1.4	1.2
Background; statistical	0.1	0.1
Background; drift	0.1	0.8
Field polarity	0.1	0.1
Relaxation	0.3	0.3
Total error TE signal	1.6	1.6

Note: The N/p-coil was used to measure both ^{14}N and proton polarizations, while the p-coils were used for proton polarization measurements only.

Water absorption of the FEP, used to cover the small NMR coils, was expected to be negligible. However, a much larger background signal was observed, compared to 1993 measurement when both bare and coated coils were used. The background signal was measured before loading the ammonia and remeasured after unloading. It contributed about 7% to the TE signal. This and the drift of the TE signal amplitude were the largest error sources in the calibration (see Table 13).

While dealing with the NMR signals of the dynamically polarized material, the main concerns were the non-linearity and NMR saturation in the uncoated coil. All the other error sources were small, as can be seen in Table 14. The non-linearity analysis is described in Section 4.4.2. It was found that for the N/p-coil the correction to be made was up to 8% while for the other coils it remained below 2%.

Another small correction was made for the shift of NMR lines due to the internal field. The response of the Q-meter was frequency dependent and the enhanced signals shifted to higher frequencies for

Table 14
Summary of enhanced proton signal errors in 1996

Error sources; proton enhanced signal	$\|\Delta P/P\|$ (%)	
	N/p-coil	p-coils
Non-linearity	2.2	0.2
Off-centering	0.1	0.1
Field polarity	0.1	0.3
Baseline fit	0.2	0.2
NMR cross-talk	0.2	0.2
NMR depolarization	1.1	0.5
Total error enhanced signal	2.5	0.8

positive polarization and to lower frequencies for negative polarization. The correction was about 0.5% at the highest polarizations. The total uncertainty of the measured proton polarization becomes thus $|\Delta P/P| = 3.0\%$ for the N/p-coil and 2.1% for the others. The coils sampled only about 15% of the volumes of the two cells. For this reason we applied a statistical sampling model which will be discussed in Section 4.5. Including the estimated sampling errors lead to an overall uncertainty of the proton polarization of the two cells together of $|\Delta P/P| = 2.7\%$.

4.4.2. Q-meter non-linearity

For Eq. (19) to hold true the Q-meter circuit must respond linearly in a wide range since the ratio of the largest proton signal to the TE signal is more than 400. Here we will show how the ammonia NMR measurements were corrected for deviations from Q-meter non-linearity. The non-linear contributions depend on the relative height, or alternatively the modulation depth $M = S(\omega_0)/V_{\text{out}}^{\min}(\chi(\omega) \equiv 0)$, that is the ratio of the absolute height of the signal divided by the minimum value of the RF-level.

Because the nitrogen magnetic moment is much smaller than that of the proton, one of the coils (N/p-coil) had a higher inductance than the proton coils to increase the signal-to-noise ratio. The proton coils were enclosed in an FEP shell to reduce the signal distortion, while the N/p-coil was not. It was also used to measure proton polarization both for SMC data taking and for the verification of the EST hypothesis. Therefore, it was of major importance to correct for the non-linearity.

In order to keep the influence of the non-linearities less than 1%, M should not exceed 0.3 for positive polarization [41,60]. The modulation of proton coils was kept below this limit (max. $-0.25/+0.2$). The modulation of the N/p-coil reached $+0.4$ and -1.2 at the highest polarization and thus exceeded the linearity limit.

The circuit was analysed as discussed before (Section 4.1). If all parameters are accurately known, we should be able to reproduce the observed Q-curves and NMR signals. As not all parameters were measured with high accuracy, we fitted the Q-curves in order to obtain more precise values of the parameters. For the fit we used the exact formula Eq. (15). The DC subtracted signal was amplified (gain G_{LF}) by a low-frequency amplifier, and it can be written as

$$V_{\text{meas}} = G_{\text{LF}} \times (\text{Re}[V(\omega, \chi)] - V_{\text{DC}}) \ . \tag{28}$$

To estimate the gain factor and the DC-offset level, a fitting function F was applied, based on the circuit parameter dependent function f, as

$$F(\omega) = af(\omega; X, R, C, L, R_{\text{coil}}, Q_{\text{c}}) - b \tag{29}$$

where $a = G_{\text{LF}} \times AV_0/R_0$, and

$$f(\omega) = \text{Re}\left[\frac{Z}{1 + XZ}\right] . \tag{30}$$

We carried out the fitting in three steps:

1. The parameters a and b were first removed by introducing the function $F'(\omega)$,

$$F'(\omega; X, R, C, L, r_{\text{c}}, Q_{\text{c}}) = \frac{F(\omega) - F(\omega_1)}{F(\omega) - F(\omega_2)} = \frac{f(\omega) - f(\omega_1)}{f(\omega) - f(\omega_2)} \tag{31}$$

in which ω_1 and ω_2 are the frequencies corresponding to the maximum (i.e., at the sweep edge) and minimum of the Q-curve. The function $F'(\omega)$ does not depend on the gain and the DC-offset, and thus could be used to determine circuit parameters.

2. The circuit parameters obtained in step 1 were fixed, and the parameters a and b were allowed to vary freely.
3. Finally, all parameters were set free and the full fitting function $F(\omega)$ was used. After these steps all fitting parameters for each coil were obtained. At each step we assigned a statistical error of 0.1 mV to every measured point and used the χ^2 minimization method.

For modulation depth measurement the minimum voltages of the unsubtracted Q-curves were measured for each coil with an oscilloscope, and these values were considered approximately equal to the DC-offset voltages. The fit agrees with the measured values within 6%.

The proton NMR line shape in ammonia is asymmetric due to interaction between the three protons within the ammonia molecule and depend on the degree of polarization. This introduces a non-linearity in the NMR measurements. The asymmetric proton line shape is discussed in detail in Ref. [30] and analysed with a simple model based on scalar proton–proton interactions within the ammonia molecule. The nitrogen–proton interaction is so weak that the polarization of ^{14}N has no influence on the proton line shape. Measured proton NMR signals are shown in Fig. 13 for positive and negative polarizations together with simulated signals based on the above indicated model. The simulation reproduced the distortions in a sufficiently satisfactory way to estimate the non-linearity of the signals. The uncertainty of the line shape, which contains the information of the signal width and height, was treated as a 20% relative error of the non-linearity corrections.

For the non-linearity estimation we had to know the filling factor of each coil, η, used in Eq. (11). However, it was very difficult to measure these values directly because they depend on the coil shape and the distribution of the material in the target cells.

We measured the Q-meter calibration constant, which is defined as the signal area obtained at 1% proton polarization. From these calibration constants and the Q-meter circuit parameters, obtained by the fitting, we could estimate the relative signal size of each coil η'_{coil}

$$\eta'_{\mathrm{coil}} = \frac{\eta_{\mathrm{coil}}\chi_{\mathrm{coil}}(\omega)}{\chi_{\mathrm{input}}(\omega)} \tag{32}$$

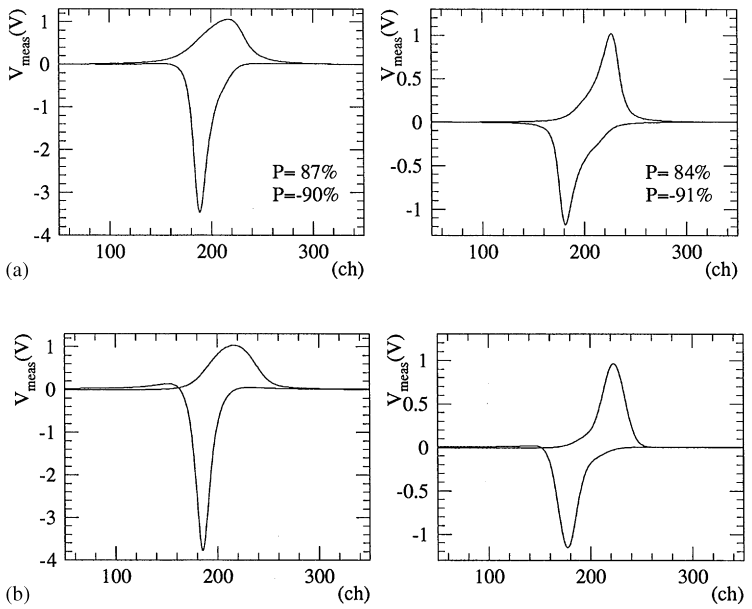

Fig. 13. (a) Measured and (b) simulated proton NMR signals of the N/p-coil (left) and of a proton coil (right).

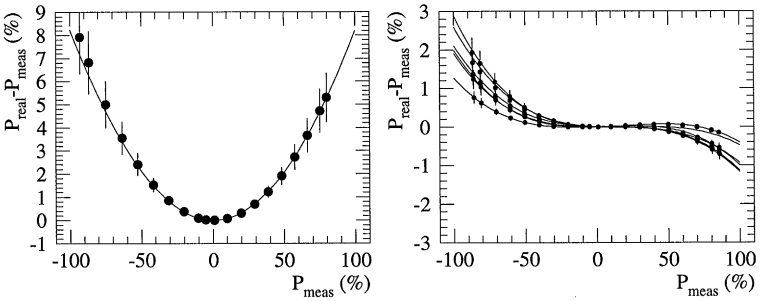

Fig. 14. Non-linearity correction $P_{\text{real}} - P_{\text{meas}}$ versus the measured polarization for (a) the N/p-coil and (b) for the proton coils.

instead of the absolute value of the filling factor η_{coil}, because we did not know the absolute susceptibility at each coil. In the Q-meter simulation the same input $\chi(\omega)$ was used for every coil, and the filling factors were corrected by η'_{coil}. Using the simulated signals (Fig. 13(b)) we calculated the non-linearity correction $P_{\text{real}} - P_{\text{meas}}$ shown in Fig. 14. The correction data were fitted to a polynomial to simplify the analysis

$$P_{\text{real}} - P_{\text{meas}} = \sum_{i=0,4} a_i \cdot P_{\text{meas}}^i \ . \tag{33}$$

At the highest proton polarization, $P \approx \pm 90\%$, the polarization of the N/p-coil was underestimated (overestimated) by about 8% for positive (negative) polarization. For the other coils the correction curve had a different behaviour, namely the polarization was overestimated by about -2% for negative, and 0.1–0.5% for positive polarizations. This difference comes from the proton signal line shape change. The uncertainty of the correction was estimated to be 20% relative due to the uncertainty in the Q-meter simulation and the crudeness of the line shape model.

However, the impact of this result on the SMC experiment was small because the overestimation of the negative polarization and underestimation of the positive polarization were largely cancelled with the two target cells having nearly the same absolute polarization and in the limit that the acceptances for both target cells were identical.

4.4.3. Measurement of the ^{14}N polarization

The ^{14}N spin system presents many problems for measuring its NMR signal because of the large quadrupole line broadening, the distance between the two quadrupole peaks of $6\omega_q/2\pi = 2.4$ MHz is too large to be covered with a single frequency sweep of the Q-meter and, correspondingly, its amplitude is very small, preventing a direct TE calibration. The measurement was carried out at two magnetic field values. Therefore, an on-line measurement of the ^{14}N polarization during DNP was not possible.

Polarizing the nuclei by dynamic cooling, which is believed to be the principal way through which DNP works in ammonia, leads to an equal spin temperature T_s among the protons and ^{14}N nuclei [61]. Then, the polarizations for the proton and for the ^{14}N spin systems are

$$P_{\text{p}} = \tanh\left(\frac{\hbar\omega_{\text{p}}}{2kT_{\text{s}}}\right), \quad P_{\text{N}} = \frac{4\tanh(\hbar\omega_{\text{N}}/2kT_{\text{s}})}{3 + \tanh^2(\hbar\omega_{\text{N}}/2kT_{\text{s}})} \tag{34}$$

neglecting the quadrupole interaction for the moment. The corrections to this formula will be discussed later.

The equal spin temperature (EST) hypothesis had not been verified beyond $|P| = 80\%$ in ammonia. There were also some conflicting results in $^{15}NH_3$ and in $^{15}ND_3$ [61–64]. Therefore, we measured the nitrogen polarization during an interruption of the SMC physics run [30].

A new technique was employed to increase the sensitivity of the NMR system for measuring the nitrogen signals. A short ($l < \lambda/4$) untuned coaxial cable was used to connect the coil to the Q-meter, instead of a tuned $\lambda/2$ cable. In this way the Q-curve becomes flatter and the effect of circuit drift is diminished, including thermal drift in the cable itself. The parameters of the NMR system are listed in Table 5 as they applied for measuring the nitrogen NMR signals.

The first-order energy levels of ^{14}N are described by Eq. (21). This formula still gives a good description of the system even though the quadrupole coupling is rather large, $\omega_q/2\pi = -0.395$ MHz [65]. Note that the sign of the quadrupole interaction is opposite to that of deuteron in butanol, reversing the order of the peaks in the NMR signal.

Since it was not possible to cover the whole signal with a single frequency sweep, only two small frequency ranges around the two peaks of the quadrupole splitted NMR spectrum were measured at two different magnetic fields. This was preferred to using two Q-meters tuned to the two frequencies at one field, because two calibrations would have to be made leading to a large error in the determination of the ratio r of the peak intensities. For most of the runs a sweep range of 300 kHz was chosen, which is sufficient to cover both peaks of the ^{14}N signal, since this shows little dipolar broadening, and to encompass the proton signal used to calibrate the ^{14}N signal. With the NMR frequency of 6.47 MHz the positions of the peaks were found at fields of 1.68 and 2.45 T. These agreed with the calculation of the energy levels in the spin-1 system, including the second-order terms [22,51]. The Q-curves were taken in the pedestal area where the absorption function did not vary strongly over the scan width. The shape of the Q-curve was measured well enough, but not its absolute magnitude. Since the pedestal was much smaller than the residual background, caused by the drifting of the NMR system, the constant could be accounted for when the nitrogen signal pieces were combined and fitted to the theoretical shape of the absorption function given by Eq. (22) with $\vartheta = \omega_q/\omega_N \approx -0.06$. The asymmetry parameter η vanishes because of the axial symmetry of the ammonia molecule.

The fitting algorithm took into account the fact that the NMR signal consists of two fragments of the spectrum and that each fragment has a different residual background since they were measured after each other with the same Q-meter. Thus, Eq. (26) was used to fit the NMR signals with different values of a_i for the two regions $\omega < \omega_N$ and $\omega > \omega_N$, but with the same values for C. The fit yields two parts of $\chi''(\omega)$, but at different magnetic fields.

Fig. 15 shows the two fragments of a signal with the fitted function. The vertical scale of the data is radically different for the two parts due to the

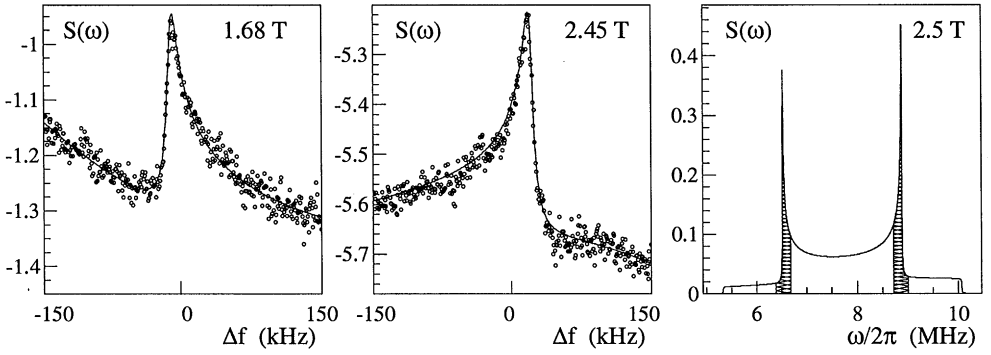

Fig. 15. *Left and centre*: The two fragments of a ^{14}N NMR signal with measured baselines subtracted over a sweep range of 300 kHz at 6.47 MHz and magnetic field of 1.68 T for $m = 0 \leftrightarrow +1$ transitions and 2.45 T for $m = -1 \leftrightarrow 0$ transitions, respectively. The solid lines are fits to the dots which are the raw data points. *Right*: The reconstructed signal at 2.5 T with the residual background removed. The hashed areas represent the measured regions. The nitrogen polarization corresponding to this signal is determined to be $P_N = 9\%$ from both the area and asymmetry methods.

drifting of the NMR system between the times when the Q-curves and signals were taken for each section of the nitrogen signal. The structure of the absorption function around the peaks is a very dominating feature and, for this reason, the absorption function can be distinguished from the background even though the Q-curve was actually taken on the pedestal of the signal. In addition to the asymmetry, r, the fit determines the other parameters of the absorption function such as A, ω_q, ω_N and C as well. Once these values were known, the full absorption function could be calculated over the whole frequency range. The complete signal reconstructed in this way is shown in Fig. 15 for a field of 2.5 T. As mentioned above, the large quadrupole splitting of the nitrogen system necessitates a more careful calculation of the nitrogen polarization in terms of the spin temperature including the second order term in Eq. (23). The correction is at most a few per mill for nitrogen polarizations of 20% and less for lower polarizations. The polarization can be directly calculated from the asymmetry parameter r using Eq. (23).

A small effect came from the fact that the projection of the spin on the solenoid field, $\langle I_z \rangle$, is smaller and $\chi''(\omega)$ is different at lower magnetic field due to the quadrupole interaction. Since the electric field gradient axis is uniformly distributed, $\langle I_z \rangle$ decreases. Thus the polarization at 1.68 T was underestimated. This effect was quantified by solving exactly for the eigenvalues and eigenstates of the Hamiltonian including quadrupole interactions. The average difference between $\langle I_z \rangle$ values calculated at 1.68 T compared to 2.45 T leads to less than a 1% relative underestimation of the polarization at 1.68 T.

Also the NMR signal is smaller at lower field values due to the quadrupole interaction [66]. Therefore, the NMR signal taken at 1.68 T is smaller by 4% compared to the NMR signal at 2.45 T. Integrating the NMR signal and multiplying by the cross-calibration constant, which was determined from a pure Zeeman system, underdetermined the polarization by about 2% relative. This was included in the systematic error.

The nitrogen NMR signal was calibrated using the proton signal at a relatively high temperature with nitrogen nuclei and protons in thermal equilibrium, which yields

$$P_N = \frac{g_p^2 I_N N_p A_N}{g_N^2 I_p N_N A_p} P_p \approx 287 \frac{A_N}{A_p} P_p \ . \quad (35)$$

The same sweep range must be used for taking NMR signals of either species for the cross-calibration to be valid because, as already mentioned, the tuning of the Q-meter depends on the frequency. The N/p-coil was calibrated with proton TE signals at 1 K by changing the field to 0.15 T where the proton Larmor frequency is 6.47 MHz. The relative error of the cross-calibration was estimated to be 2.5%.

An interesting result concerned the test of the EST theory. This was done by polarizing the protons with DNP starting from zero and continuing to the highest possible (positive and negative) value, stopping along the way to measure the nitrogen signals. The plot of the data in Fig. 16 supports an overall agreement with the EST prediction over a large range of polarizations. The small systematic deviation from EST, also observed in $^{15}NH_3$ [63,64], can be due to the solid-state effect [24]. However, for the muon scattering asymmetry $A_{\parallel}^{p}$ this deviation can be neglected as will be shown below.

The absolute error of 1% for the nitrogen polarization was found to be dominated by the uncertainty of fitting the residual background

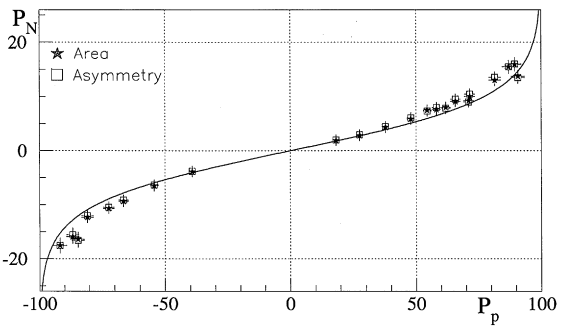

Fig. 16. A test of EST theory in ammonia material. The nitrogen polarization, as determined by the cross-calibrated area and asymmetry methods, is plotted as a function of the proton polarization. The solid line is the expected relation if the EST hypothesis is valid.

simultaneously with the line shape [30]. The effect of the background drift was studied both by comparing the successively measured signals and by using simulated signals with artificial backgrounds.

We also studied the behaviour of the spin systems during a field sweep in the FS mode to check that the field rotation would not cause cross-relaxation between the proton and nitrogen spins. This test began with a high proton polarization of about 90%. The magnetic field was reduced to 45 mT and immediately raised back to 2.5 T several times. At each of the steps, the proton and nitrogen signals were measured. Once the proton polarization fell to about 40%, DNP was started and continued until the polarization again reached $\approx 90\%$ stopping DNP for measuring the nitrogen signals. At the beginning of the decay, the polarization of the nitrogen system increased significantly, up to 40%. After the initial increase, the nitrogen polarization also began to decay. However, once DNP was started, the ammonia spin systems obeyed EST again with a time constant of about 25 min. This confirms that under DNP the spin systems are rather cooled by a common heat bath than polarized independently by the two-spin flip transitions due to the solid-state effect.

During the field rotation the minimum field was 0.5 T and therefore little cross-relaxation took place during rotation. Also, DNP was started almost always immediately after the field rotation, re-establishing EST.

The contribution of the ^{14}N polarization to the muon scattering asymmetry $A_{\parallel}^{\mathrm{p}}$ is

$$\Delta A_{\parallel}^{\mathrm{p}} = \frac{\sigma_{\mathrm{N}} P_{\mathrm{N}}}{3\sigma_{\mathrm{p}} P_{\mathrm{p}}} A_{\parallel}^{\mathrm{N}} \ . \tag{36}$$

$A_{\parallel}^{\mathrm{N}}$ has not been directly measured. However, it can be estimated by using the shell model of the ^{14}N nucleus, i.e., a ^{12}C core plus the remaining proton and neutron in a $\mathrm{p}^{1/2}$ state. It can be shown that their spins have a probability $\frac{1}{3}$ to be oriented parallel to the nuclear spin, and a probability $\frac{2}{3}$ to be oriented antiparallel to it. So, the polarization of the nitrogen nucleus corresponds to $\frac{1}{3}$ of the proton and neutron polarizations in this nucleus. The proton and the neutron together are assumed to behave like a deuteron, and thus, $A_{\parallel}^{\mathrm{N}} = -\frac{1}{3} A_{\parallel}^{\mathrm{d}}$. This yields

$$\Delta A_{\parallel}^{\mathrm{p}} = -\frac{\sigma_{\mathrm{d}} P_{\mathrm{N}}}{9\sigma_{\mathrm{p}} P_{\mathrm{p}}} A_{\parallel}^{\mathrm{d}} \ . \tag{37}$$

Using the measurement of A_1^{d} (see Eq. (1)), it was possible to evaluate the correction term on the proton asymmetry A_1^{p}. This correction is small, -0.2% to $+0.2\%$ of A_1^{p}. The residual error is found to be very small, compared to the total error on A_1^{p} calculated during the 1993 run. Using more detailed nuclear shell descriptions [67,68] has very little influence on this correction. The error due to the uncertainty on A_1^{d} is about 10 times larger than the error due to the uncertainty on P_{N}.

4.5. Accuracy of polarization measurement in a large target

In a large target it is in general not feasible to measure the polarization uniformly because of the RF field distribution of the NMR coils (see Section 3.5). Moreover, the muon beam [69] had an intensity profile resembling a gaussian with $\sigma = 12$ mm, thus weighing the material more in the centre of the target cell. In the ideal case the NMR and the beam would sample the material in the same way and the possible radial inhomogeneity of the polarization should cancel out. The beam was averaging the material in any case longitudinally so that inhomogeneity in this direction would have an effect only via the estimation of the average polarization. The NMR measurements were not uniform along the length of the target cells.

Of the plausible sources of inhomogeneity the most relevant ones during DNP were the inhomogeneity of the magnetic field, temperature gradients and microwave field gradients. During the frozen spin mode the main sources were temperature gradients, NMR depolarization and superradiance.

At this point we note that the occurrence of superradiation has been observed in our system during magnetic field ramping and large negative polarizations. The effective impedance of the NMR probe coil then has a negative real part which may provide such a large gain that the circuit starts

oscillating until the polarization is reduced or the circuit is shifted off resonance with the change of the magnetic field. The circuit has resonance frequencies in the proximity of the cable resonances corresponding to 1 to 4 half-wavelengths. At 2.5 T field the coaxial lines connecting the probe coil and the series-tuned Q-meter have electrical lengths of 5 half-wavelengths at the proton Larmor frequency (Table 5). When the field is ramped the Larmor frequency will cross the lower resonances and self-oscillation of the circuit may occur. In order to fully suppress the polarization loss due to superradiance, the magnetic field was made inhomogeneous during the field rotation procedure.

The standard homogeneity of the longitudinal field was about 3.5×10^{-5} which corresponded to a 2.5 MHz range in the microwave frequency. This was within the precision required for optimum DNP. In addition, microwave frequency modulation was always used (see Section 4.6) and, therefore, polarization inhomogeneity due to the inhomogeneity of the magnetic field could be minimized.

It was estimated that due to the Kapitza resistance of the material [70] a temperature step of about 10–30 mK occurred between the beads and helium during DNP. Inside the beads there were gradients as well but these kind of small-scale effects were averaged out by the NMR measurements. During DNP a somewhat higher temperature was expected in the centre of the target cells, depending on the efficiency of convection within the dilute mixture. In the frozen spin mode, it was observed that the upstream target cell stayed at a higher temperature. The gradients were of the order of 20 mK over a target cell. Only during the measurements of $A_\perp$ this had some significance. Over a period of about 70 h in 0.5 T a longitudinal inhomogeneity of the order of 0.5% developed due to the temperature dependence of the relaxation (see Section 5).

The radial gradient of the microwave power is a controversial subject. Since DNP is done at frequencies close to the edges of the EPR absorption line, most of the power close to the centre of the EPR line is absorbed in the outer layers of the target cell which may lead to lower polarizations in the centre. With NMR coils embedded in the material a better averaging of the polarization is achieved if such a difference in polarization occurs. The NMR coils were in most of our experiments embedded in the material to avoid this situation. In 1995 an additional Speer resistor was placed on the axis of the cell to monitor the microwave field intensity; otherwise the resistors were placed on the outside. A constant offset was found but it did not depend on the selection of the microwave frequencies in the vicinity of the optimum values. The modes in a cylindrical microwave cavity having maximum intensities on the axis could have counteracted the absorption effect to some extend.

A concern was the possibility of polarization inhomogeneity due to NMR optimization, since the setting of the microwave frequency and power was based only on the NMR polarization measurement. This opened in principle the possibility that the cell volume, not sampled by the coils, could have a lower polarization.

In performing an NMR measurement a small loss of polarization due to the saturation effect occurs mainly near the probe wire, leading to an error in the average polarization measurement. The saturation effect is related to the population changes of the nuclear spin states caused by the RF field of the NMR. This is a local effect in contrast to the sublevel population changes due to the spin-relaxation effect and the microwave field during DNP. The loss of polarization due to NMR can be shown to be of the form [71]

$$P(n) = P(0)\mathrm{e}^{-n\varepsilon} \tag{38}$$

where n is the number of frequency sweeps through the NMR absorption line (from several hundred to several thousand in the SMC target to obtain one polarization measurement), and

$$\varepsilon = \frac{\pi\gamma^2 B_1^2}{|\mathrm{d}\omega/\mathrm{d}t|}\ . \tag{39}$$

At this point it is assumed that the polarization is constant otherwise, i.e., that the target is in the frozen spin mode and that spin-lattice relaxation can be neglected. The effect of NMR depolarization is also the largest in the frozen spin mode because there is no restoring effect due to DNP. Under

these assumptions the measured polarization can in principle be calculated as

$$P_{\mathrm{meas}}(t) = P\frac{\int_V \mathrm{e}^{-t/\tau_{\mathrm{eff}}(r)} H_\perp^2(\boldsymbol{r})\,\mathrm{d}\boldsymbol{r}}{\int_V H_1^2(\boldsymbol{r})\,\mathrm{d}\boldsymbol{r}}\ . \tag{40}$$

Here r is the distance from the coil axis and the effective time constant is

$$\tau_{\mathrm{eff}}(r) = \Delta t\frac{|\mathrm{d}\omega/\mathrm{d}t|}{\pi\gamma^2 B_1^2} = \frac{\Delta t}{\varepsilon} \tag{41}$$

with Δt being the interval between the frequency sweeps. From Eqs. (40) and (41) one sees that in order to have a negligible NMR depolarization one should avoid large field strengths in the target material close to the coil wire either by increasing the diameter of the wire, by covering it with inert material, or by limiting the RF current in the coil by the choice of circuit parameters. Furthermore, the NMR measurement should not be done too often, because relaxation is extremely slow in frozen mode and because during DNP close to the maximum polarization the build-up is very slow. Also the number of frequency sweeps should be kept as low as possible. These requirements were fulfilled during our measurements.

Instead of resorting to a theoretical error analysis we measured the effect of NMR depolarization in the frozen spin mode by switching off NMR for a certain period to observe the thermal relaxation. In a period of 8 h no relaxation was observed so all polarization decay in the frozen mode could be addressed to NMR depolarization. The time spent in the frozen mode was about 24 h maximum, yielding an error of about 0.5% in the polarization measurement.

During DNP the depolarization due to NMR might have caused a constant underestimation of the polarization. To quantify this, the target was polarized for several hours with NMR switched off, starting at very high polarizations with optimum frequency and power settings. If the polarization close to the NMR coil would have become substantially smaller due to depolarization before switching off NMR, it should have recovered during this time. Thereafter we switched off the microwaves and went to frozen spin mode, freezing in the status quo. Finally, we enabled the NMR measurement again and looked for the decay of the signal as a function of time, where the closest beads should be polarized back to the steady-state value. The observed decay constants agreed with the ones found in the frozen spin mode showing that the NMR depolarization is negligible during DNP.

To estimate the uncertainty due to different target samplings by the beam and the NMR two approaches were used. In the first one we assumed that a linear radial polarization gradient existed and we calculated the error in the average polarization. The radial dependence of polarization was investigated in 1993 and 1995 by using two small-size NMR coils at different radial positions. The observed effects were small, about 2% at most, which was less than the intrinsic accuracy of polarization measurement. In 1994 the NMR coils were placed on the outer radius of the target cells, thus the material in the centre was not effectively sampled. The radial dependence of the DIS asymmetry itself was used to reveal any corresponding polarization gradients but no such a dependence was observed within the experimental accuracy. With the NMR coils placed at an effective radius of 13–14 mm a linear gradient of the polarization would not cause a bias compared to the average target polarization seen by the muon beam.

In the second method we applied the theory of random sampling [72] in order to estimate the uncertainty of the polarization of the whole target. We defined the volume sampled by each coil as the volume giving 95% of the NMR signal (see Section 3.5). In most of our experiments the sampled volumes were 40–50% of the cell volumes, except in the case of the 1996 experiment in which rather small coils were located at a 1.3 cm radius from the centre line. Each proton coil sampled about 55 cm^3 and the N/p coil 75 cm^3. With three, respectively four, NMR coils for proton polarization measurements in ammonia, the sampled volume fractions were 15% and 18% for the upstream and downstream cells, respectively. The theory of random sampling introduced a variance of the polarization estimate $\hat{P}$ of each cell, giving an additional error

$$s_{\mathrm{sampling}} = |\hat{P} - \langle P\rangle| = \frac{\sigma t\sqrt{1-f}}{\sqrt{n}} \tag{42}$$

with $\langle P \rangle$ the mean measured polarization in the upstream or downstream cell, σ the standard deviation of the measurement, n the number of samples (this is the number of coils) and t a factor taken, e.g., from the Student's t-distribution for $n-1$ degrees of freedom and a chosen probability of the confidence limit. The average standard deviations after correcting for non-linearity and off-centering were $\sigma_{\mathrm{up}} = 0.029$ and $\sigma_{\mathrm{down}} = 0.015$. With a confidence limit of 68% this lead to values of s_{sampling} of 0.020 and 0.008, respectively. Putting this together with the error of the average degrees of measured polarizations, we obtained errors of 3.1% and 2.3% of the polarization estimates for the upstream and downstream cells. The combination of both gives an error for the average polarization of 2.7%.

4.6. Polarization enhancement by frequency modulation

An important aspect for reaching high degrees of polarization by DNP is the possibility of polarization enhancement by frequency modulation (FM) of the microwaves. For materials in which the solid-state effect dominates in the polarization mechanism, it has been found that FM enhances the polarization substantially, notably if synchronized with magnetic field modulation [73]. In these cases ESR hole-burning occurs and DNP is limited by the phonon bottleneck. In materials in which nuclear cooling by thermal mixing is the dominant mechanism for DNP, such as the glassy materials used in the SMC experiments, FM is not expected to have a substantial effect [74]. The reason is that the whole ESR line is affected in the DNP due to spin–spin interactions. However, small increases (1–5%) have been reported for several hydrogen-rich glasses doped with Cr(V)EHBA [75], and for protons in propanediol and for deuterons in fully deuterated propanediol [70] also doped with the Cr(V)EHBA. In the latter case FM was applied to compensate the static magnetic field inhomogeneity. Considerable enhancements (10–20%) of protons and ^{19}F by FM have been observed by Hill et al. in various glassy materials doped with Cr(V)EHBA obtaining up to about 85% polarizations [76].

In our deuterated butanol glass FM of $\cong 30$ MHz of the microwave frequency of $\cong 70$ GHz gave rise to an unexpectedly strong enhancement of the polarization, a factor of 1.7, as shown in Fig. 17a, together with a reduction of the built-up time by a similar factor [77]. Apparently, FM altered qualitatively the behaviour of the DNP process. We studied the EPR absorption with bolometers,

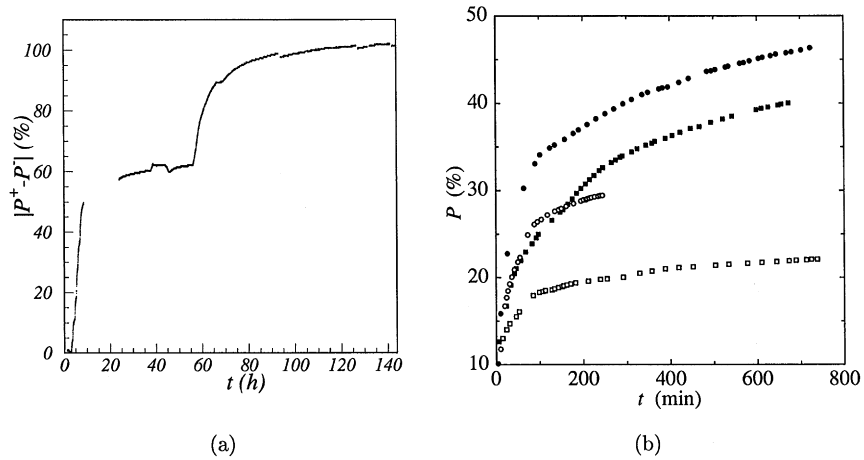

Fig. 17. (a) Effect of turning on the frequency modulation in the d-butanol target. The difference between the polarizations in the target cells is shown. At time $t = 55$ h the FM with a width of 20 MHz was switched on. (b) Deuteron polarization as a function of time with (filled symbols) and without (open symbols) the FM. *Open squares* and *circles* refer to positive and negative polarization without FM, respectively. *Closed squares* and *circles* are the same with FM on. During the data-taking the microwave power and frequencies were continuously adjusted to optimize the polarization build-up.

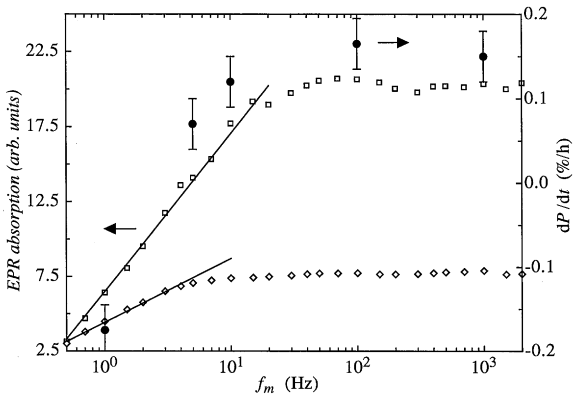

Fig. 18. *Open symbols*: Enhancement of the EPR absorption as a function of the modulating frequency for two characteristic values of the input power. The higher power level of about 0.2 mW/g (*squares*) increases the lattice temperature and this shortens the built-up time. The lower power level of about 0.1 mW/g (*diamonds*) led to higher nuclear polarization because of the lower lattice temperature. The lines are fits to the slopes. *Filled symbols*: Polarization built-up rate as a function of the modulating frequency. The data have been taken with d-butanol at polarization $P \times 50\%$.

which were carbon composite resistors situated in the microwave cavities close to the target material. These measurements showed that without FM (only 0.1 MHz band width of the EIO tube) satellite peaks occurred at the edges of the EPR line. With FM these satellite peaks disappeared [77,78]. The additional absorption increased with the modulating frequency f_m and then saturated at about $f_m = 100$ Hz (see Fig. 18). The latter allowed us to make an estimate of a characteristic period T_m of the FM effect which matches better the relaxation time $10^{-2} < \tau_1 < 10^{-1}$ s or the saturation estimate [79] than the spin–spin relaxation times.

Fig. 17b shows the typical time evolution of the deuteron polarization with and without FM. In butanol FM increased the proton polarization relatively weakly; typically from 0.75 to between 0.85 and 0.94. However, at these higher proton polarizations the reduction of the spin temperature is about the same as for deuterons.

The explanation that the effect is based on magnetic field inhomogeneity [70] can be rejected because of the good performance of our magnet and the achieved uniform nuclear polarization along the target (see Section 3.3). On the other hand, the large enhancement is not in accord with microscopic DNP theories [80] which usually deal with uniform microwave fields. One may postulate that the gain of 1.7 in the nuclear polarization in the deuterated butanol target material was induced by exciting additional "spin packets" [79] within the inhomogeneous EPR line. That should have been accompanied by a considerable increase, at least twice, of the optimum incoming microwave power. Despite this, the maximum deuteron polarization, 60%, was obtained with even a lower incoming microwave power per unit mass, namely about 0.05, instead of 0.15 mW/g which was used to achieve the maximum polarization without FM. None of these two possibilities can explain the satellites in EPR spectra either.

The observed polarization enhancement by FM has recently been interpreted by a spatially variation of the microwave field [81,82]. For simplicity plane waves along the target axis (z-direction) are assumed in this work. The real part of

$$p(z,\omega) = \mathrm{i}\frac{\mu_0}{2}\omega\chi(z,\omega)I(z,\omega) \tag{43}$$

describes the power absorbed in the target material; μ_0 is the vacuum permeability and I is the magnetic component of the microwave intensity in the cavity. With a sharp frequency a standing wave pattern with an intensity distribution along the z-axis

$$I(z,\omega) = \tfrac{1}{2}H^2\mathrm{e}^{-2L\cdot\beta(\omega-\omega_0)}\{1+\cos[2(\alpha_0 z-\alpha L)]\} \tag{44}$$

occurs. Here, H is the strength of the magnetic field component of the microwaves transverse to the magnetic field, L is the target length, and α and β are the real and imaginary parts of a complex propagation constant $k = \alpha - \mathrm{i}\beta$ which, in good approximation, can be written in terms of the susceptibility χ and the dielectric constant $\varepsilon = \varepsilon' - \mathrm{i}\varepsilon''$ as

$$k = \alpha - \mathrm{i}\beta \cong \frac{\sqrt{\varepsilon'}\omega}{c}\left[1+\frac{\chi'}{2}-\frac{\mathrm{i}}{2}\left(\chi''+\frac{\varepsilon''}{\varepsilon'}\right)\right] \tag{45}$$

if $\chi', \chi'' \ll 1$ and $\varepsilon''/\varepsilon \ll 1$. From this expression it is clear that the propagation constant α is a function of χ', with $\alpha_0 = \alpha$ ($\chi' = 0$) appearing in Eq. (44), and that the attenuation factor β is a function of χ''.

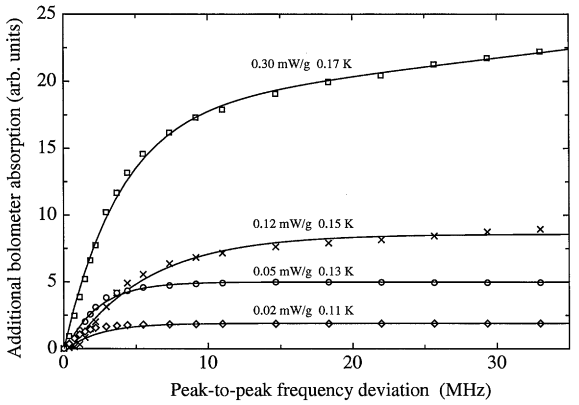

Fig. 19. Additional microwave absorption as a function of the peak-to-peak frequency deviation, measured at a frequency of 69.532 GHz. The modulation frequency was 500 Hz.

With FM the phase factor in Eq. (44) has a variation given by [81]

$$\Delta\alpha \cdot L = L \cdot \mathrm{Re}[k(+\Delta\omega/2) - k(-\Delta\omega/2)]$$

$$\cong \eta\omega \frac{\sqrt{\varepsilon'}}{2c} L \cdot \Delta\chi' \qquad (46)$$

where $\eta \approx 0.6$ is the filling factor of the target material. Assuming $\varepsilon' \approx 2$, $L = 0.6$ m, and the spectral bandwidth $\Delta\omega/2\pi = 30$ MHz due to FM, over which $\Delta\chi' \cong 0.04$, we obtain $\Delta\alpha \cdot L \cong 5\pi$. This entails a considerable spatial displacement of the interfering fringes. It is apparent that the dispersion of the target material plays the key role in this process. Fig. 19 shows the additional bolometer absorption as a function of the peak-to-peak frequency deviation with the mean frequency setting of 69.532 GHz and at four different microwave power densities. The modulation frequency was 500 Hz. The shown curves are fits based on integration of Eq. (43) over the bandwidth of the FM, and the maximum of the losses taken as free parameter [81,82].

5. Relaxation data and transverse polarization

An important issue concerns the relaxation of the proton and deuteron spins to thermal equilibrium when the microwaves are turned off. Long relaxation times are necessary to be able to carry out polarization reversals by 180° magnetic field rotations, and to do transverse spin asymmetry measurements with a fairly low magnetic field perpendicular to the muon beam.

Relaxation times of our materials were studied mainly in low magnetic fields at low temperatures, but some measurements were carried out in the 2.5 T field. Most of the relaxation data were obtained during the SMC runs, but some during the technical runs initiated to obtain information about the target properties and to carry out thermal equilibrium NMR calibrations.

As expected the relaxation times depend strongly on magnetic field and temperature. Fig. 20 shows the deuteron relaxation times versus temperature for a 0.5 T field in d-butanol. Considerable scatter occurs in these data, but the general trend is clear. Deuteron relaxation times were about 600 h at 50 mK. Proton relaxation times in butanol were measured at a number of temperatures and magnetic field values. They were longer than deuteron relaxation times, namely in the order of 1000 h in a 0.5 T field and at 50 mK. No difference in relaxation times was observed between negative and positive polarizations within the accuracy of the measurements. In ammonia the proton relaxation time, measured in a 0.5 T field at 60 mK, was about 500 h.

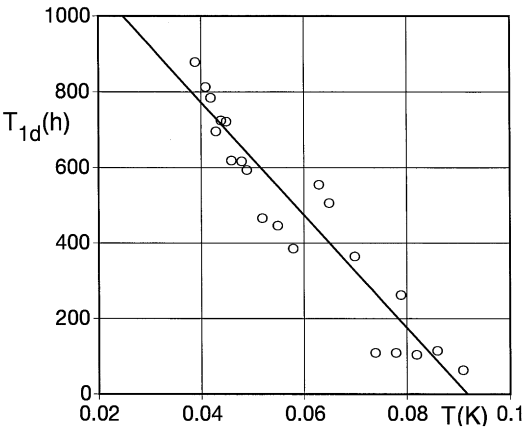

Fig. 20. Nuclear spin relaxation times T_1^d in deuterated butanol as a function of temperature T and a magnetic field of 0.5 T.

Since relaxation times were only very long in a moderate magnetic field at temperatures well below 0.1 K it was important to be able to cool our large target cells quickly. Our dilution refrigerator was designed to do so. The relaxation times were sufficiently long to have at most a small depolarization ($\approx 0.5\%$) during the 180° magnetic field rotation.

For the transverse spin asymmetry measurements the target cells were first polarized longitudinally in the 2.5 T field. After stopping DNP by turning off the microwaves, the target cooled down rapidly to well below 0.1 K. Thereafter, the magnetic field was reduced to 0.5 T followed by a 90° rotation achieved by reducing the longitudinal field simultaneously with ramping the transverse dipole field to 0.5 T. This latter field served as a holding field with the target in FS mode. Since this dipole field was unipolar, it was necessary for spin reversal in the transverse spin asymmetry measurements to go first back to longitudinal polarization in order to be able to reverse the spin directions by using microwave irradiation at the other frequency. DNP was not possible in the transverse dipole field.

Accurate NMR measurement to determine the transverse polarization was not possible, owing to the inhomogeneity of the dipole field. However, one of the small NMR coils was retuned to the lower Larmor frequency for protons in a 0.5 T field. This coil was solely used for monitoring purposes; a TE calibration was not available.

The proton relaxation time at 0.5 T and at about 50 mK was long enough to interpolate the polarization decay using a linear function which was valid to a high accuracy. The loss of polarization was only about 1% in 12 h. During the $A_\perp^p$ data taking period of 17 d with 100 GeV muons [3] the polarization was reversed 10 times, resulting in an average polarization $|P|_{av} = 80\%$.

For the deuterated target the relaxation times were shorter and in order to use the beam time most effectively the field was ramped to 0.5 T while the dilution refrigerator was still cooling down. Assuming an exponential temperature dependence of the relaxation time the polarization decay was calculated using the temperature data (see Fig. 21). The additional error due to this procedure was at most 0.5%. During the $A_\perp^d$ data taking period of 14 d with 190 GeV muons [6] the polarization was reversed five times, and the average polarization was $|P|_{av} = 42\%$.

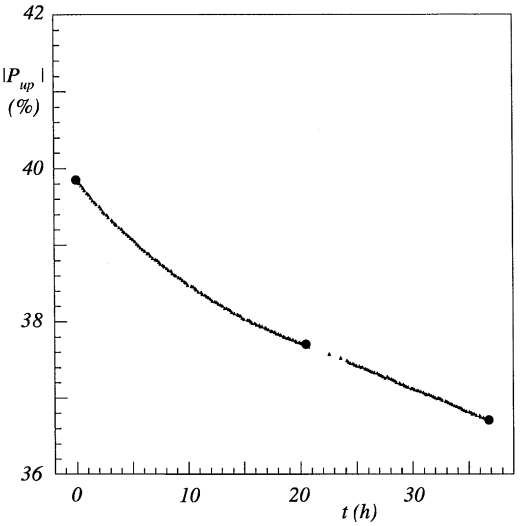

Fig. 21. An example of the relaxation of the deuteron polarization during the 1995 $A_\perp^d$ measurement in the 0.5 T transverse magnetic field. The three data points are the measured polarization values and the small dots represent the interpolated values.

6. Summary and concluding remarks

The performance of a polarized target should not be solely characterized by the maximum polarization obtained but rather by the average polarization during the data taking of the DIS experiment. To cancel false asymmetries the spin directions in our double cell target were reversed fairly often by rotating the magnetic field in an automated fashion. Further cancellation of false asymmetries was done by polarization reversals by DNP every 2 to 3 weeks. Therefore, a rapid polarization build-up was essential in order to avoid loss of beam time. This was also important to recover the polarization quickly after incidents such as power failures. Considerable effort was invested to increase the reliability and user-friendliness of the target operation. We have achieved high degrees of polarization in all of our experiments.

Typical polarization built-up curves for the butanol, d-butanol and ammonia targets are shown in

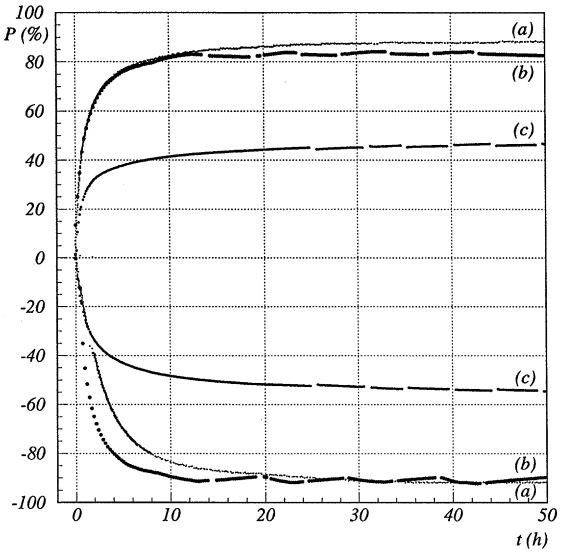

Fig. 22. Typical polarization build-up in the target materials, (a) ammonia, (b) butanol, and (c) deuterated butanol followed during 50 h. The breaks in the data sets are interruptions of the measurements due to field rotations.

Fig. 22. In all cases FM has been used. In the case of the proton target, about 95% of the maximum polarization was obtained after 10 h of DNP and the maximum was reached in 24 h. In contrast, the build-up of the deuteron polarization was much slower, as about 40 h were needed to reach 95% of the maximum values. After the initial nearly exponential growth, a very slow, almost linear, trend was seen and the maximum polarization was reached after 180 h of DNP. The microwave power was decreased in the course of DNP to lower the lattice temperature. For the ammonia target somewhat higher microwave power was needed and correspondingly the temperatures were higher.

The maximum polarizations reached with different materials are listed in Table 15. The average degrees of polarization $|P_{av}|$ and their total errors are also given. The considerably larger polarization time constant of ammonia is probably due to the lower density of paramagnetic centres. The average polarization depends also on external factors such as the number of polarization reversals and cannot be directly used to compare the materials. As an example, $|P^+ - P^-|_{av}$ during the 1995 data taking is shown in Fig. 11.

The lower polarization of the deuteron target is compensated by the higher dilution factor. The nuclear spin temperatures corresponding to these polarization values are about 1 mK for the deuterated target materials. The fact that the negative polarization is higher can be qualitatively understood in the framework of the spin temperature theory [83], by the observation that the shape of the EPR absorption line is steeper on the high-frequency side.

Our polarized target with a thickness of 6.8×10^{24} polarized nucleons per cm^2 is the largest ever used. It was the only means to reach satisfactory statistical accuracy with the limited intensity of the muon beam.

For the NMR measurements we have analysed the Q-meter circuit very carefully and gained understanding of the non-linearities and the corrections involved. An effort was made to accurately measure the proton and deuteron polarizations with several coils in each cell. Although the NMR coils did not sample the complete cell volumes, we showed that the additional error by this incomplete sampling was small, and that we determined in all SMC measurements the target polarizations with a 3% relative error or better.

Table 15
Average polarizations $P_{av} = |P^+ - P^-|/2$ and their total errors for the different target materials, together with the built-up time $\tau_{0.7}$ to reach 70% of the maximum polarizations P^+_{max} and P^-_{max}

Material	P_{av} (%)	$\Delta P_{av}/P_{av}$ (%)	$\tau_{0.7}$ (h)	P^+_{max} (%)	P^-_{max} (%)
Butanol	86	3.2	1.5	+ 94	− 94
d-Butanol	51	2.0	2.5	+ 51	− 60
Ammonia	89	2.7	3.5	+ 89	− 91

The frequency modulation (FM) effect, discovered in 1992 in the refurbished EMC target, increased the deuteron polarization by a factor of 1.7 and allowed us to reach a record deuteron polarization of -60% at 2.5 T.

We have measured the ^{14}N polarization carefully, confirming that the EST hypothesis was closely valid in the ammonia material in a 2.5 T field. The corrections to the measured deep inelastic scattering asymmetries were estimated more precisely than in earlier work [84,85].

In the future, a similar target design will be employed by the COMPASS collaboration [86] to search for the gluon contribution to the nucleon spin. The superconducting magnet will be replaced by a new one with a much larger opening angle to track particles with high transverse momenta. In addition, the target diameter will be smaller by a factor of 2 owing to a better focusing of the muon beam. ^{6}LiD might be introduced as the deuteron material because of its larger fraction of polarizable nucleons compared to deuterated alcohols or ammonia.

References

[1] SMC, B. Adeva et al., Phys. Lett. B 302 (1993) 533.
[2] SMC, D. Adams et al. Phys. Lett. B 329 (1994) 399; Erratum, Phys. Lett. B 339 (1994) 332.
[3] SMC, D. Adams et al., Phys. Lett. B 336 (1994) 125.
[4] SMC, D. Adams et al., Phys. Lett. B 357 (1995) 248.
[5] SMC, B. Adeva et al., Phys. Lett. B 369 (1996) 93.
[6] SMC, D. Adams et al., Phys. Lett. B 396 (1997) 338.
[7] SMC, B. Adeva et al., Phys. Rev. D 56 (1997) 5330.
[8] SMC, B. Adeva et al., Phys. Lett. B 412 (1997) 414.
[9] SLAC E142, P.L. Anthony et al., Phys. Rev. Lett. 71 (1993) 959.
[10] SLAC E142, P.L. Anthony et al., Phys. Rev. D 54 (1996) 6620.
[11] SLAC E143, K. Abe et al., Phys. Rev. Lett. 74 (1995) 346.
[12] SLAC E143, K. Abe et al., Phys. Rev. Lett. 75 (1995) 25.
[13] SLAC E143, K. Abe et al., Phys. Lett. B 364 (1995) 61.
[14] SLAC E143, K. Abe et al., Phys. Rev. Lett. 76 (1996) 587.
[15] SLAC E154, K. Abe et al., Phys. Rev. Lett. 79 (1997) 26.
[16] SLAC E154, K. Abe et al., Phys. Lett. B 404 (1997) 377.
[17] HERMES, K. Ackerstaff et al., Phys. Lett. B 404 (1997) 383; Phys. Lett. B 442 (1998) 484.
[18] S.C. Brown et al., in: W. Meyer (Ed.), Proceedings of Fourth International Workshop on Polarized Target Materials and Techniques, Bad Honnef, Germany, 3–6 September 1984, p. 102.
[19] SMC, B. Adeva et al., Nucl. Instr. and Meth. A 349 (1994) 334.
[20] J. Kyynäräinen (on behalf of SMC), Nucl. Instr. and Meth. A 356 (1995) 47.
[21] A. Abragam, M. Goldman, Rep. Prog. Phys. 41 (1978) 395.
[22] A. Abragam, Principles of Nuclear Magnetism, Clarendon Press, Oxford, 1961.
[23] W. de Boer, Dynamic Orientation of Nuclei at Low Temperatures, CERN Yellow Report 74-11, 1974; J. Low Temp. Phys. 22 (1976) 185.
[24] W. Meyer et al., Nucl. Instr. and Meth. 227 (1984) 35.
[25] M. Krumpolc, J. Roček, J. Am. Chem. Soc. 101 (1979) 3206.
[26] M. Krumpolc, D. Hill, H.B. Stuhrmann, in: W. Meyer, E. Steffens, W. Thiel (Eds.), Proceedings of Nineth International Symposium on High Energy Spin Physics, Vol. 2, Bonn, 1990, Springer, Berlin, 1991, p. 340.
[27] S. Bültmann et al., Nucl. Instr. and Meth. A 356 (1995) 102.
[28] W. Meyer et al., Nucl. Instr. and Meth. 215 (1983) 65.
[29] S. Brown et al., in: W. Meyer (Ed.), Proceedings of Fourth International Workshop on Polarized Target Materials and Techniques, Bad Honnef, Germany, 3–6 September 1984, p. 66.
[30] SMC, B. Adeva et al., Nucl. Instr. and Meth. A 419 (1998) 60.
[31] O.V. Lounasmaa, Experimental Principles and Methods Below 1K, Academic Press, London, 1974, p. 265.
[32] T.O. Niinikoski, Nucl. Instr. and Meth. 192 (1982) 151.
[33] T.O. Niinikoski, J.-M. Rieubland, in: K. Yasukochi, H. Nagano (Eds.), Proceedings of Nineth International Cryogenic Engineering Conference (ICEC9), Butterworth, Guilford, UK, 1982, p. 580.
[34] T.O. Niinikoski, in: K. Mendelssohn (Ed.), Proceedings of Sixth International Cryogenic Engineering Conference (ICEC6), Grenoble, France, 11–14 May 1976, p. 102.
[35] J.-M. Le Goff et al., Nucl. Instr. and Meth. A 356 (1995) 96.
[36] A. Daël et al., IEEE Trans. Magn. 28 (1992) 560.
[37] R.H. Dicke, Phys. Rev. 93 (1954) 99.
[38] Yu.F. Kisselev et al., Zh. Eksp. Teor. Fiz. 94 (2) (1988) 344 [Sov. Phys. JETP 67 (1988) 413].
[39] J.F.M. van Gelder, M.Sc. Thesis, Delft Univ. of Technology, June 1991.
[40] S. Ishimoto et al., in: W. Meyer, E. Steffens, W. Thiel (Eds.), Proceedings of Nineth International Symposium on High Energy Spin Physics, Vol. 2, Bonn, 1990, Springer, Berlin, 1991, p. 369.
[41] G.R. Court, D.W. Gifford, P. Harrison, W.G. Heyes, M.A. Houlden, Nucl. Instr. and Meth. A 324 (1993) 433.
[42] T.O. Niinikoski, A. Rijllart, Nucl. Instr. and Meth. A 199 (1982) 485.
[43] N. Hayashi et al., Nucl. Instr. and Meth. A 356 (1995) 91.
[44] S.D. Dhawan, IEEE Trans. Nucl. Sci. NS-39 (1992) 1331.
[45] S.D. Dhawan et al., IEEE Trans. Nucl. Sci. NS-43 (1996) 2128.
[46] T.O. Niinikoski (representing SMC), Nucl. Instr. and Meth. A 356 (1995) 62.
[47] T.O. Niinikoski, in: G.R. Court, S.F.J. Cox, D.A. Cragg, T.O. Niinikoski (Eds.), Proceedings of the Second

Workshop on Polarized Target Materials, Report RL-80-080, SRC, Rutherford Laboratory, 1980, p. 80.
[48] Yu.F. Kisselev, C.M. Dulya, T.O. Niinikoski, Nucl. Instr. and Meth. A 354 (1995) 249.
[49] J.D. Jackson, Classical Electrodynamics, 2nd Edition, Wiley, New York, 1975, p. 311.
[50] G. Arfken, Mathematical Methods for Physicists, 3rd Edition, Academic Press, New York, 1985, p. 425.
[51] C.M. Dulya, Ph.D. Thesis, University of California, Los Angeles, 1996.
[52] C.M. Dulya, Nucl. Instr. and Meth. A 356 (1995) 88.
[53] Y.K. Semertzidis, Nucl. Instr. and Meth. A 356 (1995) 83.
[54] C.M. Dulya et al., Nucl. Instr. and Meth. A 398 (1997) 109.
[55] O. Hamada et al., Nucl. Instr. and Meth. 189 (1981) 561.
[56] G.D. Wait et al., Nucl. Instr. and Meth. A 274 (1989) 515.
[57] F. Sperisen, Nucl. Instr. and Meth. A 260 (1987) 455.
[58] M.H. Cohen, F. Reif, Nuclear quadrupole effects in solids, in Solid State Physics, Vol. 5, Academic Press Inc., New York, 1957.
[59] D. Krämer on behalf of SMC, Nucl. Instr. and Meth. A 356 (1995) 79.
[60] J.J. Hill, D.A. Hill, Nucl. Instr. and Meth. 116 (1974) 269.
[61] G.R. Court, W.G. Heyes, Nucl. Instr. and Meth. A 243 (1986) 37.
[62] G.R. Court, W.G. Heyes, W. Meyer, W. Thiel, in: W. Meyer (Ed.), Proceedings of the Fourth International Workshop on Polarized Target Materials and Techniques, Bad Honnef, Germany, 1984, p. 53.
[63] D.G. Crabb, D.B. Day, Nucl. Instr. and Meth. A 356 (1995) 9.
[64] B. van den Brandt, J.A. Konter, S. Mango, M. Wessler, in: W. Meyer, E. Steffens, W. Thiel (Eds.), Proceedings of the Nineth International Symposium on High Energy Spin Phys., Vol. 2, Springer, New York, 1991, p. 307.
[65] S.S. Lehrer, C.T. O'Konski, J. Chem. Phys. 43 (1965) 1941.
[66] C.M. Dulya, J. Kyynäräinen, Nucl. Instr. and Meth. A 406 (1998) 6.
[67] R.L. Huffman et al., Phys. Rev. C 35 (1987) 1.
[68] H.W. Baer et al., Phys. Rev. C 12 (1975) 921.
[69] N. Doble et al., Nucl. Instr. and Meth. A 343 (1994) 351.
[70] S. Ishimoto, S. Hiramatsu, S. Isagawa, A. Masaike, K. Morimoto, Jpn. J. Appl. Phys. 28 (1989) 1963.
[71] A. Abragam, M. Goldman, Nuclear Magnetism: Order and Disorder, Clarendon Press, Oxford, 1982, p. 295.
[72] W.G. Cochran, Sampling Techniques, Wiley, New York, 1977, p. 27.
[73] A. Abragam et al., in: G. Shapiro (Ed.), Proceedings of Second International Conference on Polarized Targets, Berkeley (USA), 30 August–2 September 1971, p. 247.
[74] H.W. van Kesteren, W.T. Wenckebach, J. Schmidt, Chem. Phys. Lett. 121 (1985) 440.
[75] D. Hill et al., in: W. Meyer (Ed.), Proceedings of Fourth International Workshop on Polarized Target Materials and Techniques, Bad Honnef, Germany, 3–6 September 1984, p. 84.
[76] D. Hill et al., Nucl. Instr. and Meth. A 277 (1989) 319.
[77] Yu.F. Kisselev on behalf of SMC, Nucl. Instr. and Meth. A 356 (1995) 99.
[78] SMC, B. Adeva et al., Nucl. Instr. and Meth. A 372 (1996) 339.
[79] A.M. Portis, Phys. Rev. 91 (1953) 1071.
[80] M. Goldman, Spin Temperature and Nuclear Magnetic Resonance in Solids, Clarendon Press, Oxford, 1970.
[81] Yu.F. Kisselev, T.O. Niinikoski, Preprint CERN-PPE/96-146, 1996.
[82] Yu.F. Kisselev, T.O. Niinikoski, in: C.W. de Jager, T.J. Ketel, J.E.J. Oberski, P.J. Mulders, M. Oskam-Tamboezer (Eds.), Proceedings of 12th International Symposium on High Energy Spin Physics SPIN96, Amsterdam, World Scientific Publ. Co., Singapore, 1997, p. 389.
[83] M. Borghini, Phys. Rev. Lett. 20 (1969) 419.
[84] EMC, J. Ashman et al., Phys. Lett. B 206 (1988) 364.
[85] EMC, J. Ashman et al., Nucl. Phys. B 328 (1989) 1.
[86] COMPASS proposal, Report CERN/SPSLC 96-14, SPSLC/P 297, 1996; addendum CERN/SPSLC 96-30, SPSLC/P 297 Add. 1, 1996.